Dalton Transactions

ROYAL SOCIETY OF CHEMISTRY

PAPER

View Article Online
View Journal | View Issue

Cite this: *Dalton Trans.*, 2025, **54**, 7641

Effects of de-fluorination on hydrophobicity and on CO_2 and CH_4 adsorption under high humidity in MeMOFs, methylated analogues of FMOFs†

Rashida Yasmeen, [a] Sheikh M. S. Islam, [b] Olajumoke M. Ayeni, [b] Peyman Z. Moghadam, [c] Jincheng Du *[a] and Mohammad A. Omary *[b]

Herein, we report carbon dioxide (CO_2) and methane (CH_4) adsorption behavior in MeMOFs, methylated analogues of FMOFs with $-CF_3$ groups replaced with $-CH_3$, utilizing grand canonical Monte Carlo (GCMC) simulations at 288, 298, and 308 K and $P \leq 40$ bar and density functional theory (DFT) computations of adsorption energies. Isosteric heats of adsorption (Q_{st}), Henry's constants (K_H) and interaction energies were used to analyze the adsorbate–adsorbent interaction strengths and gas uptake of guest molecules. The Q_{st} of CO_2 was found to be 1.29–1.73 times higher in MeMOF-1 than in FMOF-1, *vs.* 1.30–1.47 times for CH_4, hence demonstrating higher guest affinity to MeMOF-1 than to the FMOF-1 polymorph. Simulated isotherms were further fitted with Langmuir, Langmuir–Freundlich, and Tóth models to calculate the isosteric heat of adsorption at infinite dilution (Q_{st0}) using the Clausius–Clapeyron equation. The data were then compared with those obtained from force-field-based Monte Carlo (MC) simulations to determine the consistency. The Tóth model presented excellent characterization of CO_2 and CH_4 adsorption, implying both FMOF-1 and MeMOF-1 materials have inhomogeneous surfaces. The order of the Q_{st0} values obtained using the Clausius–Clapeyron equation was consistent with that obtained from MC simulations and confirmed the higher uptake of CO_2 and CH_4 in MeMOF-1 as predicted by GCMC. The presence of H_2O vapor, up to 80% relative humidity, did not affect the CO_2 and CH_4 adsorption in MeMOF-1 structures, as was observed in the analogous FMOF-1 parent structure. The larger pore size and surface area upon substituting $-CF_3$ groups with $-CH_3$ groups allow for significantly greater CO_2 and CH_4 uptake in MeMOFs compared to FMOFs with no water uptake even at high humidity. These simulations were applied upon MeMOF analogues of multiple FMOF-1 polymorphs known to date and are thus expected to hold for MeMOF analogues of other FMOF and MOFF structures reported by the Omary and Miljanić teams, respectively. Experimental data have validated the superhydrophobic nature of the MeMOF-1 composition *via* a polymorphic form with a different topology, MeMOF-2, attaining an ~100° increase in water-drop contact angles, from ~74° for a control plastic substrate to ~172° upon dry-coating it with MeMOF-2. Experimentally synthesized MeMOF-2 possesses the same {Ag(3,5-$(CH_3)_2$-1,2,4-triazolate)} empirical formula as that of simulated MeMOF-1 structures, albeit with a different crystal structure and lower porosity.

Received 29th January 2025,
Accepted 17th March 2025

DOI: 10.1039/d5dt00242g

rsc.li/dalton

1. Introduction

Global warming and climate change are adverse consequences of CO_2, CH_4, and other greenhouse gas emissions.[1] The CO_2 concentration in the atmosphere has been noticeably increasing over time, mainly because of the combustion of fossil fuels.[2–5] Natural gas, which is predominantly composed of CH_4, has been proposed as a promising alternative to other fossil fuels (*e.g.*, gasoline and coal) since its combustion produces ~50% less CO_2. However, this overlooks other environmental impacts of the hydraulic fracturing (*i.e.*, fracking) process including the depletion and contamination of water

[a]*Department of Materials Science & Engineering, University of North Texas, 1155 Union Circle, Denton, Texas-76203, USA. E-mail: Jincheng.Du@unt.edu*
[b]*Department of Chemistry, University of North Texas, 1155 Union Circle, Denton, Texas-76203, USA. E-mail: Omary@unt.edu*
[c]*Department of Chemical Engineering, University College London, London WC1E 7JE, UK*

†Electronic supplementary information (ESI) available: Optimized geometry of $-CH_3$-functionalized MOFs; interaction parameters; adsorption isotherm fitting details; isosteric heats of adsorption; Henry's constant; adsorption selectivity (PDF). See DOI: https://doi.org/10.1039/d5dt00242g

resources. Nevertheless, the presence of CO_2 and N_2 in natural gas along with the more desired CH_4 decreases the energy production efficiency and also adds to the challenges of using this technology.[6,7] Consequently, CO_2 capture and separation from CH_4 represent significant scientific and technological challenges with both environmental and economic implications.[8] Amine scrubbing,[9,10] membrane separation,[11,12] and solid adsorbent separation[13–15] are the three most widely used methods for CO_2 removal. Metal–organic frameworks (MOFs) have been garnering significant attention over the traditional porous materials, such as silica, activated carbons, and zeolites for selective carbon capture, due to their unique geometrical structures and tunable chemical properties.[16–19] In order to enhance CO_2 adsorption by MOFs, several methods have been considered, such as creating narrow pores by structural interpenetration,[20,21] adjusting pore chemistry through cation exchange,[22–24] introducing "open" (coordinatively unsaturated) metal sites,[25,26] and modifying the pore surface by ligand functionalization.[27–32] According to Li *et al.*, ligand functionalization is a promising approach to tune the adsorbate–adsorbent interaction,[23] which could enhance CO_2 adsorption in MOFs without significantly altering the overall structure of the parent MOF. However, pore structure, porosity, and pore surface functionality could be greatly impacted by functionalization and should be considered when designing MOF functionalization. Additionally, two more important factors, such as hydrophobicity of the MOFs' structure and their selective CO_2 and CH_4 adsorption capacities over water should be accounted in designing MOFs for enhanced CO_2 and CH_4 adsorption, as the presence of water in humid or aqueous environments can adversely affect CO_2 and CH_4 uptakes in MOFs.[33–36]

Fluorous metal–organic frameworks, such as the most heavily-investigated FMOF-1 composition $Ag_2[Ag_4Tz_6]$, where Tz = 3,5-$(CF_3)_2$-1,2,4-triazolate, are superhydrophobic MOFs whose CO_2 uptake is not affected by the presence of water vapor at all.[37] In this work, the ligand functionalization effect of $-CH_3$ group upon CO_2 and CH_4 adsorption in MeMOF analogues of FMOF structures has been investigated using grand canonical Monte Carlo (GCMC) simulations. FMOF-1 was considered as the parent structure. To the best of our knowledge, CO_2 adsorption in FMOF-1 at 298 K was studied previously,[37] but neither CH_4 adsorption nor the effect of functionalization has been investigated before. As such, the aims of this study are two-fold: (1) to study the effect of functionalization by $-CH_3$ instead of $-CF_3$ groups on CO_2 and CH_4 adsorption in the resultant hypothetical MeMOF-1 structures at three different temperatures (288, 298, and 308 K) up to 40 bar and (2) to examine the hydrophobicity and selectivity of CO_2 and CH_4 over water in the resultant MeMOFs *vs.* their parent FMOF counterparts. We simulated the CO_2 and CH_4 adsorption in both the parent and methyl-functionalized FMOFs and investigated Henry's constant (K_H) and the isosteric heat of adsorption at infinite dilution (Q_{st0}) in order to understand the adsorbate–adsorbent interactions. These energy parameters, acquired during the simulation were compared with the K_H values obtained using the Tóth isotherm model and the Q_{st0} values derived from the Clausius–Clapeyron equation. By comparing the results, we concluded that the substitution of $-CH_3$ for $-CF_3$ can greatly improve the CO_2 and CH_4 adsorption capacity in MeMOF-1, even at wet conditions. The GCMC-predicted large increase in CO_2 or CH_4 adsorption in MeMOF-1 *vs* FMOF-1 structures is counteracted by merely subtle compromise in water rejection, hence resulting in not just similar but indeed greater CO_2/H_2O and CH_4/H_2O selectivity in MeMOFs *vs*. FMOFs. The selective adsorption of CO_2 and CH_4 over water and the hydrophobicity of the structures were examined under high relative humidity conditions (RH = 80%). Overall, the computational findings in this work may pave the way for discovering new experimental compositions that could be promising alternatives to fluorinated hydrophobic materials. This predictive work, therefore, represents the first step towards the development of a new chemical composition for fluorine-free adsorbents, coatings, or additives that may prove promising in the national/international effort to find alternatives to Teflon, FMOF, ZIF, per- and polyfluoroalkyl substances (PFAS), and other hydrophobic materials without compromising their pertinent desired properties and uses (indeed, with potential improvement).

This work aims to investigate the impact of de-fluorination of fluorinated metal–organic frameworks, by replacing F atoms with H atoms (*e.g.*, $-CF_3 \rightarrow -CH_3$) in some known structures, on the water-rejection ability of the resulting frameworks during CO_2 and CH_4 adsorption. Though the focus herein is on some polymorphic forms of FMOF-1 among those known to date to attain methylated counterparts (MeMOFs), this strategy is expected to be applicable to other FMOF and MOF structures reported by the Omary[38,39] and Miljanić[40–44] research teams, respectively. This work represents the first predictive step toward the development of alternatives to other classes of hydrophobic and/or omniphobic materials (ZIFs, COFs, FMOFs, MOFFs, PFAS, *etc.*) being investigated for such attributes.

2. Methodologies

2.1 Adsorbent model

Yang *et al.* first synthesized FMOF-1, which consists of a perfluorinated structure.[45] FMOF-1c is the first adsorbent in this study, which was obtained at 290 K and 61 bar under a carbon dioxide stream, with CO_2 guest molecules manually removed.[37] FMOF-1c (Fig. 1a) has a tetragonal crystal structure with the $I\bar{4}2d$ space group and lattice parameters $a = b =$ 14.0733 Å, c = 37.675 Å, $\alpha = \beta = \gamma = 90°$. Considering FMOF-1c as the primary structure, MeMOF-1c was constructed by replacing the $-CF_3$ groups with $-CH_3$ while retaining the parent FMOF-1c 3D structure. After the replacement, the preliminary MeMOF-1c structure was optimized using the Forcite module of Material Studio,[46] as shown in Fig. S1 and S2 (ESI†). The universal force field,[47] which describes bonded and nonbonded interactions between the framework atoms, was considered during structure optimization. The final MeMOF-1c (Fig. 1b) structure was obtained after completing the two-step optimization process. We followed the same procedures for

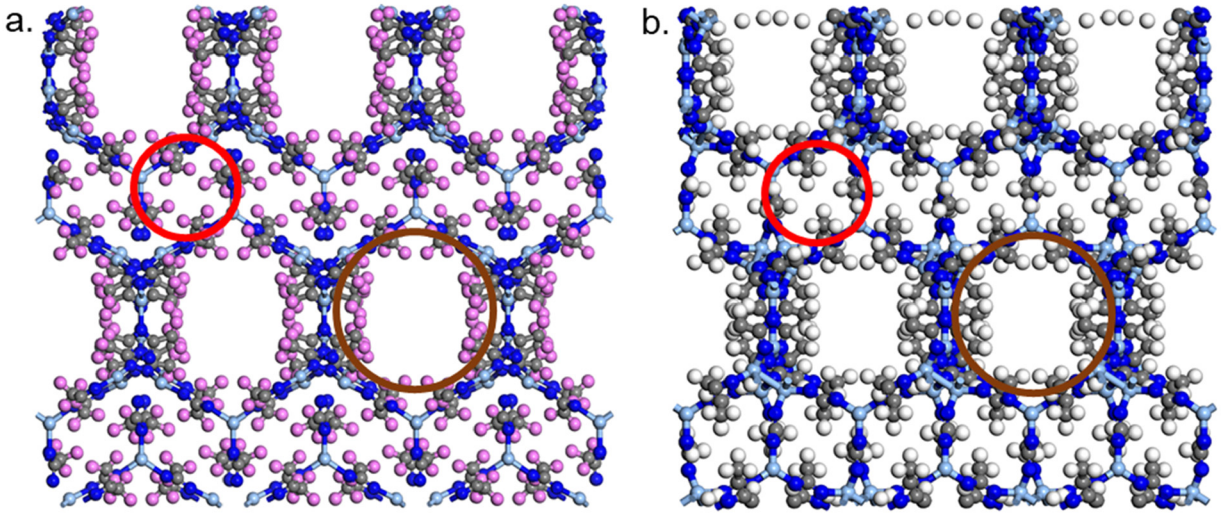

Fig. 1 Crystal structures of (a) FMOF-1c and (b) MeMOF-1c. Color code – Ag: cyan, F: pink, N: blue, C: gray, and H: white.

Table 1 Geometric properties of the MOF structures studied in this work

Structure	Density (g cm^{-3})	Surface area (m^2 g^{-1})	Void fraction	Pore volume (cm^3 g^{-1})	Channel diameter (Å)
FMOF-1a	1.76[a]	817[a]	0.40[a]	0.22[a]	6.20[a]
MeMOF-1a	1.26[a]	1338[a]	0.48[a]	0.39[a]	6.44[a]
FMOF-1b	1.61[a]	903[a]	0.44[a]	0.28[a]	6.80[a]
MeMOF-1b	1.27[a]	1304[a]	0.46[a]	0.36[a]	6.21[a]
FMOF-1c	1.66[a]	826[a]	0.41[a]	0.25[a]	6.73[a]
	—	782[b]	0.41[b]	—	6.30[b]
	1.76[c]	842[c]	0.40[c]	0.23[c]	—
MeMOF-1c	1.24[a]	1425[a]	0.53[a]	0.42[a]	6.67[a]

[a] This work. [b] Moghadam *et al.*[37]. [c] Babarao *et al.*[69].

the optimization of MeMOF-1a and MeMOF-1b (Fig. S3 and S4†), which represent analogous modifications of FMOF-1a and FMOF-1b structures that correspond to the structures of FMOF-1 obtained under vacuum at 100 K and under a nitrogen stream at 90 K, respectively (with N_2 molecules manually removed from the FMOF-1b structure). Material Studio has the efficiency to generate feasible crystal structures, and many researchers have used this software to characterize MOF structures prior to their synthesis.[48–50] MeMOF-1c has a tetragonal crystal structure with the $I\bar{4}2d$ space group and lattice parameters $a = b = 13.1532$ Å, $c = 37.2022$ Å, $\alpha = \beta = \gamma = 90°$. Both FMOF-1c and MeMOF-1c possess two types of pores: smaller and larger. Smaller pores are marked by a red circle, whereas larger pores are denoted by a brown circle (Fig. 1). The geometrical properties of the structures are shown in Table 1 and Table S2.† The energy of the initial structure and the optimized MeMOF-1c structure is compared in Table S1.†

2.2 Interaction potential

To study the CO_2 and CH_4 adsorption in the pertinent MOFs herein, we employ theoretical models of the adsorbates and adsorbent and a force field that illustrates the adsorbate–adsorbent energetic interactions.[51] A combination of short-range Lennard-Jones (LJ) and long-range Coulomb potentials was used to describe the non-bonded interactions, as shown in eqn (1):

$$V_{ij} = 4\varepsilon_{ij}\left[\left(\frac{\sigma_{ij}}{r_{ij}}\right)^{12} - \left(\frac{\sigma_{ij}}{r_{ij}}\right)^{6}\right] + \frac{q_i q_j}{4\pi\varepsilon_0 r_{ij}} \quad (1)$$

where the interacting atoms are indicated by i and j, r_{ij} is their interatomic distance, q_i and q_j are the partial atomic charges of i and j, respectively, ε_{ij} and σ_{ij} are the LJ potential parameters describing the well depth and repulsion distance between i and j, and ε_0 is the dielectric constant. The LJ parameters for the framework atoms were taken from the universal force field (UFF).[47,52] The Lorentz–Berthelot mixing rules[53] were used to calculate the ε and σ parameters between different atom types. A cutoff length of 12.8 Å was considered for all LJ interactions and the tail corrections were ignored. Partial atomic charges are responsible for electrostatic interactions. The long-range electrostatic interactions were calculated using the Ewald summation method.[54] The partial charges of $-CF_3$ groups in FMOF structures were taken from the work of Dalvi *et al.*,[55] whereas those for the remaining FMOF atoms were taken from Moghadam *et al.*'s work.[37] In the functionalized structures (MeMOF-1a, MeMOF-1b, and MeMOF-1c), the partial charges of $-CH_3$ groups were calculated using the connectivity-based atom contribution method (CBAC) described by Xu and Zhong.[56] CO_2 was considered as a linear three-site rigid model with a C–O bond distance of 1.16 Å, following the TraPPE force field.[57] CH_4 was considered as a spherical single-site model. The LJ parameters and the partial charges of the framework atoms and adsorbates are listed in Tables S3–S5.† The Lennard-Jones parameters of CH_4 guest molecules were taken from the TraPPE model,[58] while water was

described using the TIP4P model.[59] The simulation box consisted of a supercell (2 × 2 × 1 unit cell) with periodic boundary conditions in all three directions for both structures. The MOFs were considered as rigid, meaning all framework atoms remained fixed during the GCMC simulation. To explore the effect of framework flexibility on the adsorption properties, we performed simulations on three different MeMOF-1 crystal structures.

2.3 Simulation details

Grand canonical Monte Carlo (GCMC)[53] simulations were performed using the RASPA2 code[60] to study CO_2 and CH_4 adsorption isotherms. For each GCMC run, the number of gas molecules in the adsorbed phase was allowed to fluctuate, while the chemical potential (μ), volume (V), and temperature (T) were kept constant. The isotherms were obtained by changing the pressure (P) and calculating the average number of adsorbed molecules (n) as an output of the simulations. Each MC simulation included random insertion, deletion, rotation, and translation with equal probabilities. Fugacities and bulk densities of CO_2 and CH_4 were calculated using the Peng–Robinson[61] equation of states. Excess adsorption isotherms were simulated by considering the void fraction of both the structures (details can be found in the ESI†). At each pressure point, 1.0×10^5 cycles were used for equilibration, followed by another 1.0×10^5 cycles to determine the adsorption properties of both CO_2 and CH_4. For pure and mixed water simulations, 5.0×10^5 cycles were used for equilibration followed by another 5.0×10^5 cycles for production runs.

The isosteric heat of adsorption at infinite dilution and the change in the heat of adsorption with pressure were calculated using eqn (2) and (3), respectively:

$$Q_{st0} = -\Delta H = \langle U_{hg} \rangle - \langle U_h \rangle - \langle U_g \rangle - RT \quad (2)$$

$$\Delta H = \frac{\langle U \times N \rangle_\mu - U_\mu \langle N \rangle_\mu}{\langle N^2 \rangle_\mu - \langle N \rangle_\mu{}^2} - \langle U_g \rangle - RT \quad (3)$$

where $\langle U_{hg} \rangle$, $\langle U_h \rangle$, and $\langle U_g \rangle$ are the average energy of a single guest molecule inside the host, the average energy of the host, and the average energy of a single guest molecule in the gas phase, respectively. N is the number of adsorbates in the system. Henry's constants (K_H) for CO_2 and CH_4 were determined using the Widom insertion method[62] with 100 000 configurationally biased insertions. K_H values were also obtained from the slope of the isotherms generated using the Tóth parameters in the low-pressure regime. By applying the parameters a_T, b_T, and m acquired from the Tóth fit, we generated loading (n)–pressure (p) data in the low-pressure region, where there is a linear relation between n and p. Energy minimization for a single adsorbate molecule inside FMOF-1c and MeMOF-1c was performed to investigate the contributions of van der Waals and coulombic interactions to the adsorption energy. Baker's minimization method[63,64] was employed for 100 independent minimization attempts, with a stopping criterion of an RMS gradient of 1.0×10^{-6}. The geometrical properties of the MOFs such as density, void fraction, pore volume, and channel diameter were computed using Zeo++ software.[65] The RASPA2 simulation code[60] was used to run all GCMC simulations.

The selective adsorption of CO_2 and CH_4 over water in FMOF-1c was calculated using Henry's constant ratio (eqn (4)) and from the GCMC simulations (eqn (5)).

$$S_{Henry} = \frac{K_{H,\,adsorbate}}{K_{H,\,H_2O}} \quad (4)$$

where $K_{H,\,adsorbate}$ and $K_{H,\,H_2O}$ are Henry's constants of the adsorbate (CO_2 or CH_4) and water, respectively.

$$S_{GCMC} = \frac{(q_{CO_2}/p_{CO_2})}{(q_{H_2O}/p_{H_2O})} \quad (5)$$

where q_i is the uptake of component i in mol kg^{-1} and p_i is the partial pressure of component i in Pa.

To validate the force field used in this study, we first simulated the CO_2 adsorption in FMOF-1c at 298 K and compared it with previously simulated data (Fig. S5 and S6†).[37] Our simulated data give rise to intermediate uptake and Q_{st} magnitudes between previously reported isotherms while exhibiting similar trends and adsorption profiles. The isosteric heat of adsorption data showed better agreement with experimental data at very low loading but started to deviate around 2.305 mol kg^{-1}.

Density functional theory (DFT) utilizing the B97D/CEP-31G functional/basis set combination was used to calculate the interaction energies. For self-consistent field (SCF) convergence, we set the convergence criteria to 10^{-N}, meaning that the convergence was achieved when the root-mean-square (RMS) change in the density matrix was less than 10^{-8} and the maximum change in the density matrix was less than 10^{-6}. The calculations were performed using the Gaussian 16 code;[66] further computational details can be found in section 3.5.

2.4 Experimental details for synthesis and contact angle measurements

MeMOF-2 is formed by the coordination of the ligand 3,5-dimethyl-1,2,4-triazolate to silver(I) ions, creating a three-dimensional coordination polymer network. The pure MeMOF-2 sample in this study was synthesized by modifying the method reported by Zhai *et al.* in 2009.[67] A mixture of a 1 : 1 molar ratio of 3,5-Me_2(1,2,4-TzH) and $AgNO_3$ (97.1 mg : 169.9 mg) was dissolved in 10 mL of methanol. To this, 5 mL of NH_4OH was added to de-protonate the triazole. The resultant solution was refluxed at 55 °C for 72 h. The precipitate was filtered, washed with cold ethanol and allowed to dry in air to obtain a pure sample. Contact angle measurements were performed for a dry-coated surface of a 1 cm × 1 cm polyethylene terephthalate (PET) plastic substrate after sanding it with a 3M pro-grade precision P220 abrasive, following a procedure described by Chen *et al.*[68]

3. Results and discussion

3.1 Adsorption isotherms

Pure component CO_2 and CH_4 adsorption isotherms were simulated for FMOF-1c and MeMOF-1c at 288, 298, and 308 K under pressures up to 40 bar. All simulation results are reported as excess quantities unless otherwise specified. Fig. 2 shows the CO_2 and CH_4 uptake of FMOF-1c and MeMOF-1c. The CO_2 and CH_4 uptake was found to be much higher in MeMOF-1c than in FMOF-1c, with the uptake of CO_2 exceeding that of CH_4 in both materials at all temperatures. The results show the effect of temperature on CO_2 and CH_4 adsorption capacities of the MOF structures. For both FMOF-1c and MeMOF-1c, CO_2 and CH_4 uptake decreases with the increase in temperature, as expected for most porous materials. The CO_2 adsorption trend is found to be different from that of CH_4, as our GCMC simulations indicate a gradual increase in CO_2 uptake up to 20 bar, followed by a plateau. In contrast, CH_4 exhibits almost linear isotherms up to 10 bar and does not saturate at 10 bar (in the case of MeMOF-1c) or even at 35 bar (in the case of FMOF-1c), consistent with the excellent experimental compressibility reported for this material upon extrapolating the experimental uptake from 0–55 bar to 300 bar using the Tóth equation.[70]

Fig. 3a shows a comparison of CO_2 and CH_4 adsorption isotherms of FMOF-1c and MeMOF-1c at 298 K. A sharp rise in CO_2 uptake is observed for MeMOF-1c up to 10 bar, whereas FMOF-1c exhibits a continuous increase in CO_2 uptake up to 20 bar and then gradually saturates. However, these GCMC simulations suggest a nearly linear increment of CH_4 uptake in the low-pressure region for both structures. The sharp rise in CO_2 uptake indicates a stronger CO_2–MeMOF-1c interaction than that of CO_2–FMOF-1c. MeMOF-1c shows higher adsorption capacities for both CO_2 and CH_4 than FMOF-1c at 298 K. Similar trends are observed at the other two temperatures simulated herein (288 and 308 K), as shown in Fig. S7 and S8.†

When computing gas adsorption isotherms in MOFs, accounting for electrostatic interactions between gas molecules and framework atoms is crucial. To account for electrostatic interactions, we must assign charges to the framework atoms. We have studied the influence of point charges on CO_2 adsorption in FMOF-1c at 298 K (Fig. S5†). CO_2 was selected for our study as it possesses a permanent quadrupole moment, whereas CH_4 is a zero-quadrupole-moment material. Consequently, CO_2 adsorption is sensitive to the charges of framework atoms, unlike CH_4 adsorption. In this study, FMOF-1c is considered the reference material, while MeMOF-1c is its methylated analogue. For CO_2 adsorption isotherms in FMOF-1c, we used the charges from a previous simulation,[37] whereby $-CF_3$ charges were taken from Dalvi *et al.*[55] But for MeMOF-1c, we used charges derived using the connectivity-based atom contribution (CBAC) method of Xu and Zhong[56] for the $-CH_3$ group. This method assigns charges to representative atoms of MOF building blocks with the same bonding environment. To ensure consistency in our analysis, we used CBAC charges[56] for $-CF_3$ to simulate CO_2 adsorption isotherms in FMOF-1c and compared the results (Fig. S5†) with our previous simulations. We observed a trend in the CO_2 adsorption isotherm of FMOF-1c similar to those in both our previous simulation and experimental data, indicating that the CBAC charge method has been validated for simulating the CO_2 adsorption isotherm in MeMOF-1c. We then studied the influence of point charges on CO_2 adsorption for MeMOF-1c at 298 K (Fig. 3b) using two different charge methods: CBAC[56] and the extended charge equilibration (EQeq) method of Wilmer *et al.*[71] (by assigning point charges that minimize an energy function that describes properties such as electronegativities or ionization potentials specifically developed/optimized for MOFs). We observed a similar trend for those isotherms with little variation in CO_2 uptake, which suggests that both methods are validated. Though different charge methods might yield different predictions for the amount of gas uptake,

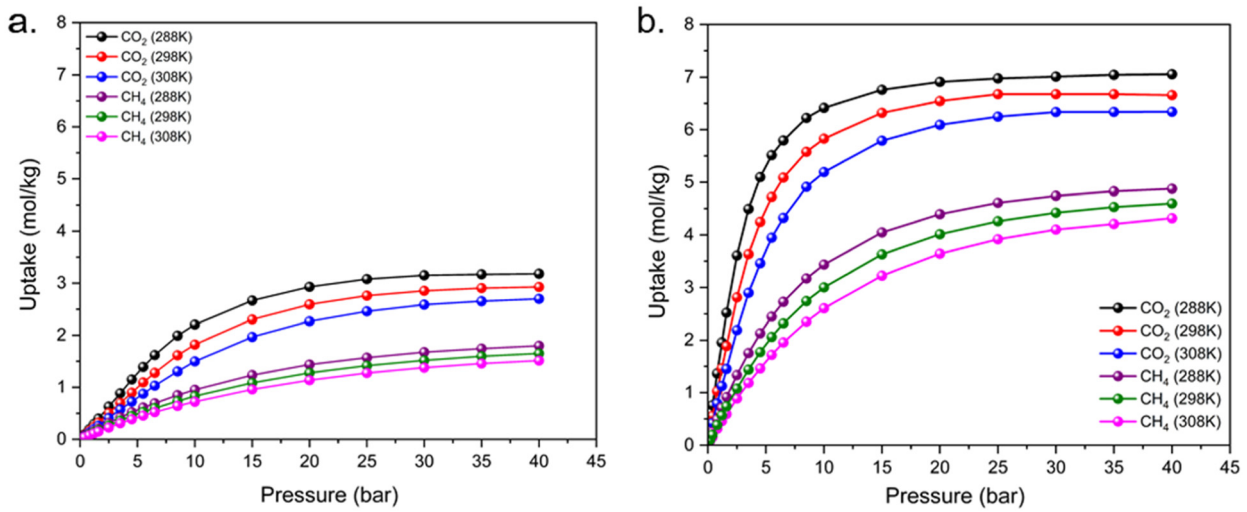

Fig. 2 CO_2 and CH_4 adsorption isotherms of (a) FMOF-1c and (b) MeMOF-1c at 288, 298, and 308 K.

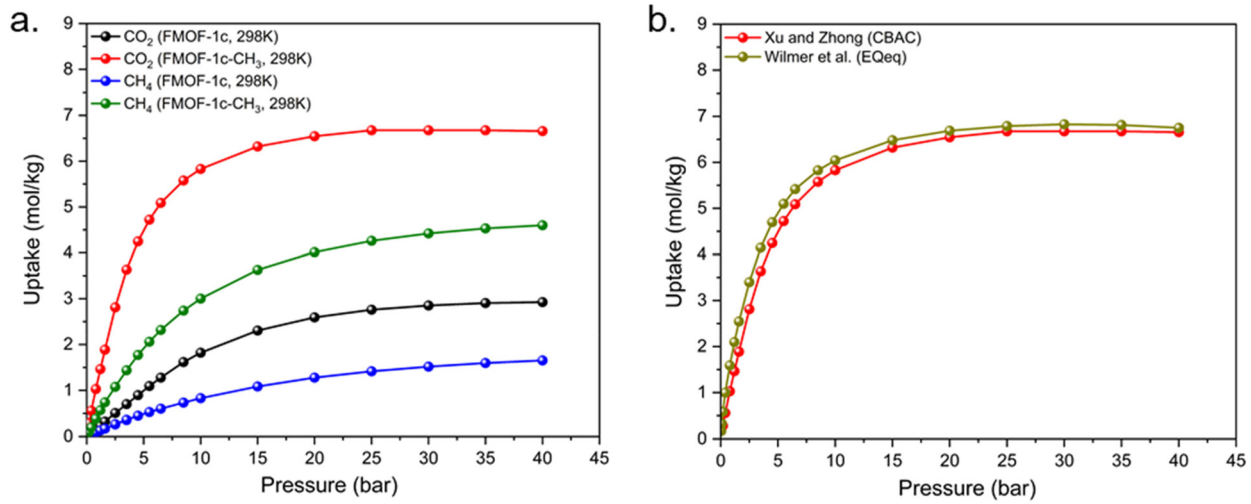

Fig. 3 (a) Comparison of CO_2 and CH_4 adsorption isotherms of FMOF-1c and MeMOF-1c at 298 K. (b) CO_2 adsorption isotherms of MeMOF-1c using two different charge methods at 298 K.

we did not observe any significant differences in the CO_2 adsorption isotherms of MeMOF-1c.

In order to achieve a qualitative molecular-level perspective on the guest molecules' adsorption behavior in each of the two MOFs, snapshots of CO_2 and CH_4 adsorption obtained from GCMC simulations at 298 K under different pressures are shown in Fig. 4 and 5, respectively. According to Fig. 4, at low pressure, CO_2 and CH_4 are preferentially adsorbed in the large cylindrical channel of FMOF-1c. As the pressure increases, the guest molecules start to emerge near the small-cavity region. When the pressure is increased further, both the cylindrical channel and the small cages become gradually populated, as per these GCMC simulations. It is worth mentioning that the small cavities are not accessible in FMOF-1c at 278 K, as per the simulation by Moghadam *et al.*[37] For MeMOF-1c shown in Fig. 5, it can be observed that both the guest molecules exhibit occupancy near the small-cavity area at low pressure, in contrast to FMOF-1c. Gradually, as the pressure increases, the cylindrical channels and the small cages become filled.

We also simulated the CO_2 and CH_4 adsorption isotherms in MeMOF-1a and MeMOF-1b and compared them with the values obtained for MeMOF-1c at 298 K (Fig. S9†). As shown in Fig. S9,† greater CO_2 and CH_4 uptake is observed for MeMOF-1c (expanded structure under a CO_2 atmosphere) compared to MeMOF-1a (rigid, guest-free, reference structure) or MeMOF-1b (expanded structure under a N_2 atmosphere). While comparing the adsorption capacities of MeMOF-1b and MeMOF-1c, we notice that MeMOF-1c exhibits significantly higher CO_2 uptake than MeMOF-1b. We speculate that this is due to the higher surface area of MeMOF-1c (1425 $m^2\ g^{-1}$) compared to that of MeMOF-1b (1308 $m^2\ g^{-1}$).

3.2 Isosteric heats of adsorption, Q_{st}

The isosteric heat of adsorption (Q_{st}) values at each pressure point were directly obtained during the adsorption isotherm simulations. The adsorption amount could be predicted by the magnitude of the isosteric heat of adsorption. The Q_{st} values for CO_2 and CH_4 adsorption in FMOF-1c and MeMOF-1c at 298 K are shown in Fig. 6. In particular, Fig. 6a compares Q_{st} for CO_2 and CH_4 adsorption as a function of uptake, whereas Fig. 6b presents Q_{st} as a function of pressure at 298 K. It is apparent that, for both structures, the Q_{st} value of CO_2 is larger than that of CH_4. So, the order of isosteric heat of adsorption is CO_2 > CH_4, consistent with the order of the adsorption capacity. The Q_{st} value of CO_2 for FMOF-1c rises evenly from ~14 to 23 kJ mol^{-1} (at 298 K), which slightly underestimates the reported Q_{st} values of CO_2 for FMOF-1c (Fig. S6†). The Q_{st} values of CH_4 also exhibit an increasing trend from ~11 to 14 kJ mol^{-1} for FMOF-1c. This increase is probably due to the lateral interactions of the guest molecules with the rise in pressure (or the adsorbate concentration).[72–74] On the other hand, the Q_{st} value of CO_2 adsorption for MeMOF-1c first declines from 24 to 22 kJ mol^{-1}, up to around 2.5 mol kg^{-1} (Fig. 6a) or 1.2 bar (Fig. 6b). After that, it increases rapidly. This indicates that CO_2–MeMOF-1c interactions dominate adsorption at low loading levels, whereas the contribution of CO_2–CO_2 interactions escalates after preferential site occupation. The Q_{st} values of CH_4 adsorption remain almost unchanged over the entire pressure range due to adsorption site saturation.[75,76] For MeMOF-1c, we observe a larger number of guest molecules (both CO_2 and CH_4) than for FMOF-1c, resulting in a higher condensed phase at a particular pressure compared to FMOF-1c. Subsequently, the isosteric heats of adsorption of both CO_2 and CH_4 for MeMOF-1c are larger than that for FMOF-1c. Since Q_{st} values are lower than 40 kJ mol^{-1}, CO_2 and CH_4 adsorption in the considered MOF structures is a physisorption process.[77] The Q_{st} values at the other two temperatures are depicted in Fig. S10–S12.†

We also studied the Q_{st} of CO_2 and CH_4 adsorption for MeMOF-1a and MeMOF-1b and compared them with MeMOF-1c data at 298 K (Fig. S14†). Table 2 displays the Q_{st0} values of the CO_2 and CH_4 adsorbates at 298 K. For all the

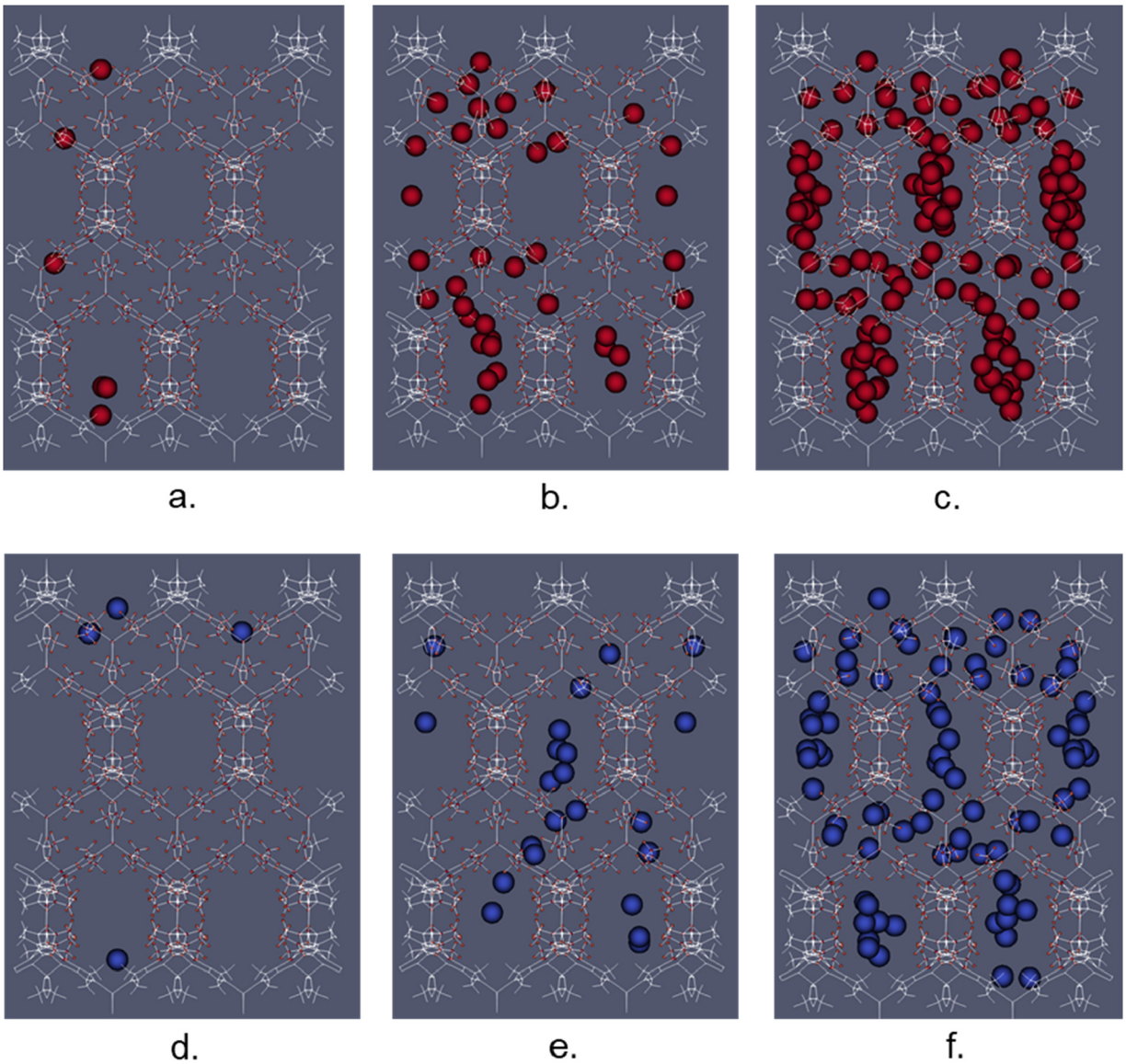

Fig. 4 Snapshots at 1, 5, and 40 bar, respectively, of FMOF-1c for (a–c) CO_2 occupancy (red spheres) and (d–f) CH_4 occupancy (blue spheres).

adsorbents, the Q_{st} values of CO_2 adsorption initially exhibit a decreasing trend up to 1.4 mol kg^{-1} (corresponding to 2 bar) and then an increasing trend. The Q_{st} values of CH_4 adsorption remain almost unchanged throughout the entire loading/pressure range. According to Fig. S14,† MeMOF-1c exhibits higher Q_{st0} values compared to the other two adsorbents, for both CO_2 and CH_4. Generally, smaller pores of porous materials display higher Q_{st} values, as smaller pores have shorter distances between the pore walls that result in stronger adsorbate–adsorbent interactions.[78,79] The highest Q_{st} values at low loading for MeMOF-1c are due to the strong adsorption of adsorbates (CO_2 and CH_4) in the small-cavity region (Fig. 5). While comparing the Q_{st} values for MeMOF-1a and MeMOF-1b, we observed that MeMOF-1b exhibits higher values than MeMOF-1a. We speculate that this is due to the smaller small-pore diameter of MeMOF-1b (6.21 Å) than that of MeMOF-1a (6.44 Å), even though the large-channel diameters show the opposite trend.

The adsorbate–adsorbent interaction strength can also be characterized by studying the heat of adsorption at infinite dilution, Q_{st0}. A stronger interaction between the gas adsorbate molecule and the host MOF material is reflected by a greater Q_{st0}.[80] Likewise, Henry's constant, K_H, can indicate the adsorbate affinity to the adsorbent. A larger K_H value represents a greater affinity of the adsorbate. Both K_H and Q_{st0} were estimated using the Widom insertion method, and the results are presented in Fig. 7a and b, respectively.

The Henry's constant of CO_2 in the studied MOFs was found to be about 1.5-fold larger than that of CH_4, whereas the isosteric heats of adsorption at infinite dilution for CO_2 was around 1.2-fold larger compared to CH_4. According to this finding, the order of the affinity is CO_2 > CH_4, which could be

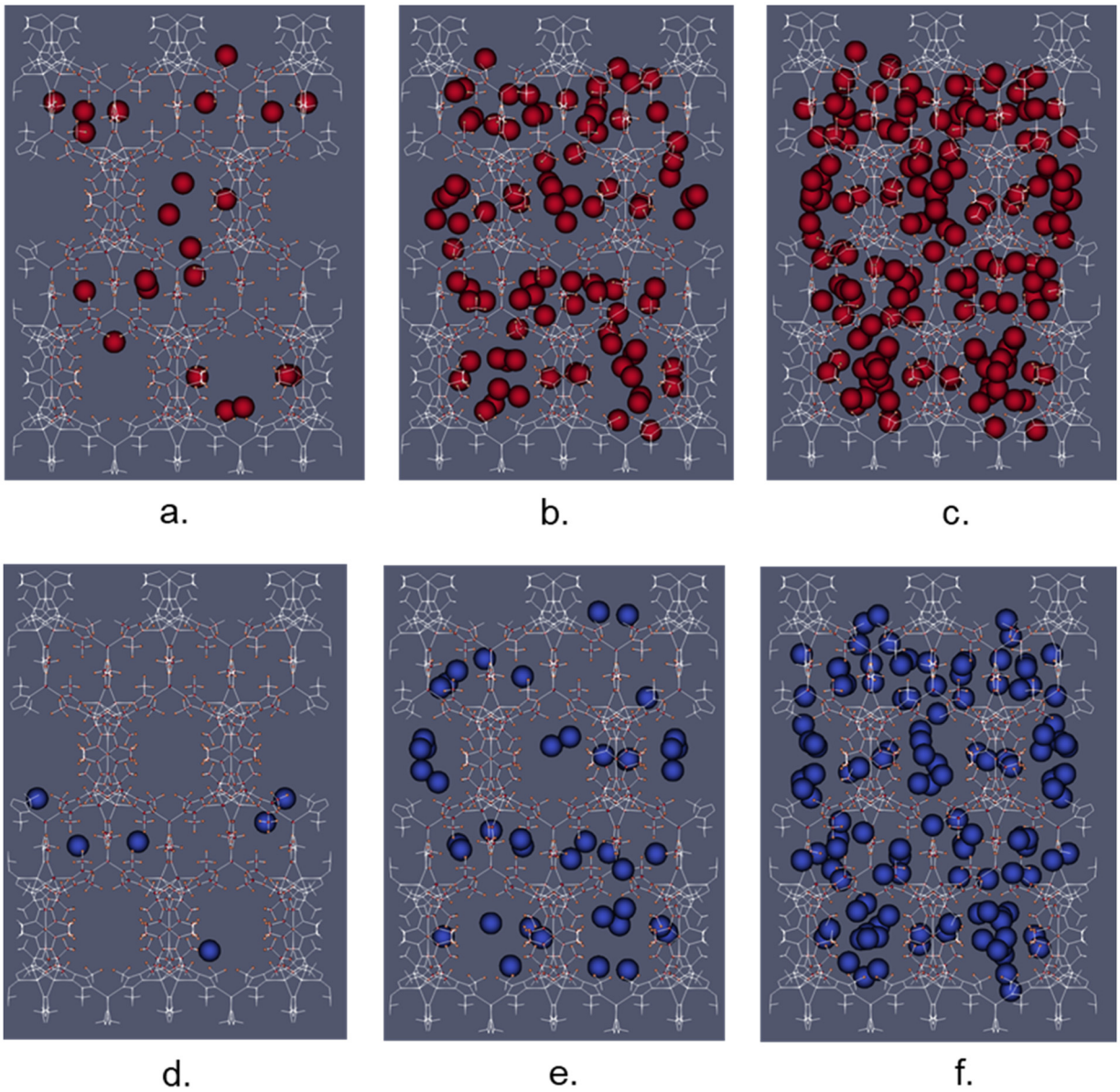

Fig. 5 Snapshots at 1, 5, and 40 bar, respectively, of MeMOF-1c for (a–c) CO_2 occupancy (red spheres) and (d–f) CH_4 occupancy (blue spheres).

due to the permanent quadrupole moment of the CO_2 molecule that generates an electrostatic force.[80] The K_H values for CO_2 adsorption in MeMOF-1c were found to be more sensitive to temperature changes in comparison with FMOF-1c, decreasing slowly with increasing temperature. At 298 K, the K_H and Q_{st0} values for CO_2 adsorption in FMOF-1c are 1.81×10^{-6} mol kg^{-1} Pa^{-1} and 13.71 kJ mol^{-1}, respectively. The corresponding values obtained for CO_2 adsorption in MeMOF-1c are 1.56×10^{-5} mol kg^{-1} Pa^{-1} and 24.51 kJ mol^{-1}, respectively. Likewise, our MC simulations (Widom insertion) predict larger K_H and Q_{st0} values for CH_4 adsorption in MeMOF-1c than in FMOF-1c. Hence, it can be concluded that CO_2 and CH_4 exhibit greater affinity and stronger interaction strength in MeMOF-1c than in FMOF-1c, which can be attributed to the methyl group ligand functionalization.

Fig. S15† displays the percentage increase of both CO_2 and CH_4 uptake and the isosteric heat of adsorption at infinite dilution as a result of $-CH_3$ functionalization in MeMOF-1c. The $(N_{MeMOF\text{-}1c} - N_{FMOF\text{-}1c})/N_{FMOF\text{-}1c}$ ratio was used to calculate the percentage increase in adsorption. Here, $N_{MeMOF\text{-}1c}$ and $N_{FMOF\text{-}1c}$ denote the amounts of adsorbates adsorbed in functionalized (MeMOF-1c) and parent (FMOF-1c) MOFs, respectively, at 1 bar and 298 K. For the isosteric heat of adsorption at infinite dilution, the comparison was made *via* the $(Q_{st0\text{-}MeMOF\text{-}1c} - Q_{st0\text{-}FMOF\text{-}1c})/Q_{st0\text{-}FMOF\text{-}1c}$ ratio, where $Q_{st0\text{-}MeMOF\text{-}1c}$ and $Q_{st0\text{-}FMOF\text{-}1c}$ represent the isosteric heat for the methyl-functionalized MeMOF and the parent FMOF, respectively.

The larger uptake of CO_2 in MeMOF-1b compared to MeMOF-1a at the low-pressure region (Fig. S9†) could be

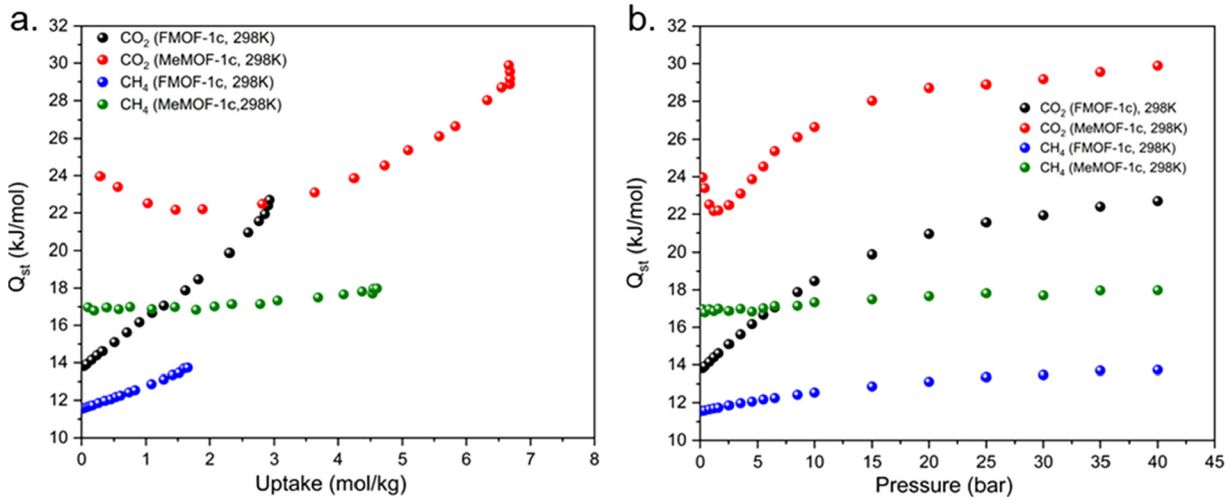

Fig. 6 Simulated isosteric heats of adsorption, Q_{st}, for CO_2 and CH_4 of FMOF-1c and MeMOF-1c: (a) as a function of uptake and (b) as a function of pressure at 298 K.

Table 2 Q_{st0} values for CO_2 and CH_4 adsorption in methyl-functionalized MeMOFs, structural analogues of FMOF structures

	Q_{st0} (kJ mol^{-1})	
Adsorbent	CO_2	CH_4
MeMOF-1a	20.20	14.16
MeMOF-1b	21.36	15.08
MeMOF-1c	24.51	17.02

explained by the K_H values for CO_2 at 298 K (Fig. S16†). Since K_H characterizes adsorbate–adsorbent interactions while ignoring adsorbate–adsorbate interactions, the larger K_H for CO_2 in MeMOF-1b indicates stronger CO_2–MeMOF-1b interaction compared to CO_2–MeMOF-1a interaction, resulting in higher CO_2 uptake in MeMOF-1b up to around 5 bar, where adsorbate–adsorbent interactions play the dominant role in CO_2 adsorption.

3.3 Interaction energy effects

The interaction energy contributions to the adsorption mechanism of CO_2 and CH_4 in FMOF-1c and MeMOF-1c at 298 K, as presented in Fig. 8 and S17–S26,† are consistent with the discussion in section 3.2. The percentage contribution of the guest–guest and host–guest interaction energies to the total energy shows that the host–guest interaction energy decreases with increasing pressure up to 40 bar. In contrast, the guest–guest interaction energy increases during CO_2 and CH_4 adsorption for both structures, up to a pressure of 40 bar.

Fig. S27† shows the relative contributions of van der Waals (vdW) and coulombic interactions to the total adsorption energy of CO_2 and CH_4 in FMOF-1c and MeMOF-1c. The inter-

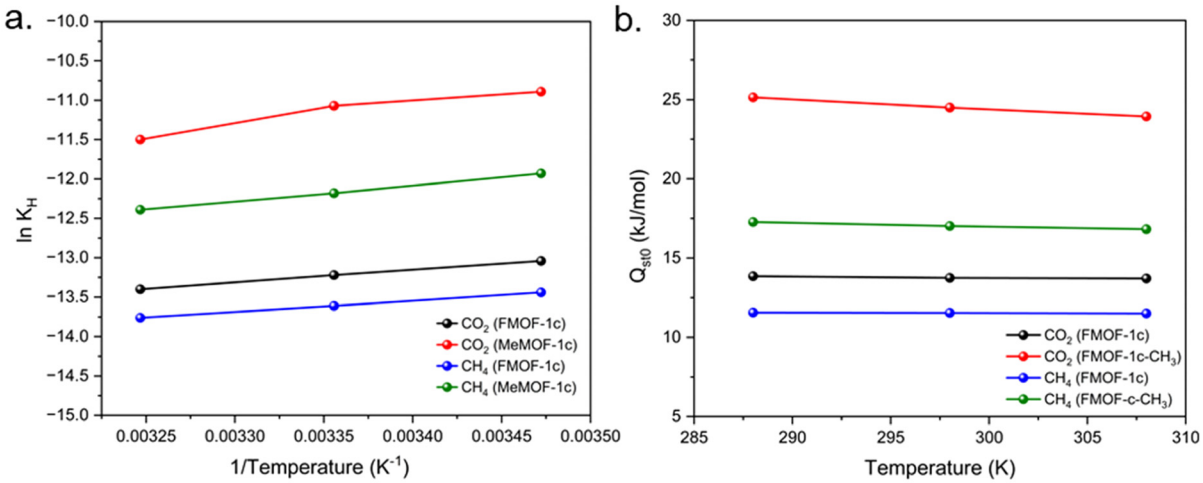

Fig. 7 (a) Henry's constant, K_H, and (b) isosteric heat of adsorption at infinite dilution, Q_{st0}, for CO_2 and CH_4 at various temperatures in MeOF-1c and FMOF-1c structures, obtained from the Widom insertion method.

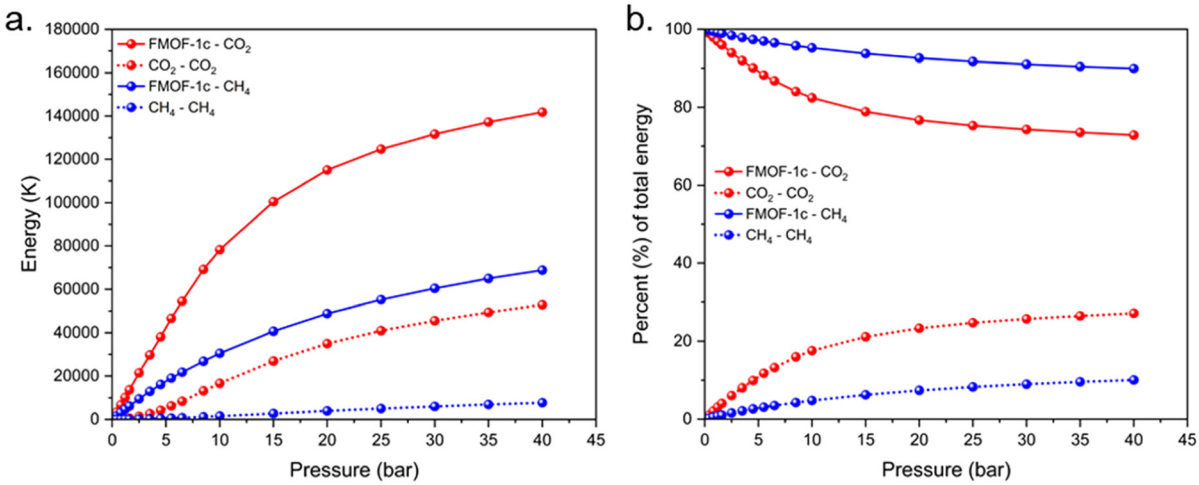

Fig. 8 The breakdown of (a) total potential energy and (b) percentage of total potential energy into host–guest and guest–guest contributions for CO_2 and CH_4 adsorptions in FMOF-1c, obtained from GCMC simulations at 298 K.

action of CO_2 is significantly stronger than that of CH_4 in analogous FMOF and MeMOF structures. Additionally, MeMOF-1c exhibits stronger interactions than FMOF-1c for both CO_2 and CH_4 adsorptions. The CH_4 model used in our simulations has no charges. Therefore, no electrostatic interactions are present among the CH_4 molecules and MOF atoms. Consequently, the adsorption energy for CH_4 arises purely from van der Waals interactions. For CO_2, on the other hand, the collective interaction consists of both vdW and coulombic interactions, with the coulombic interaction contribution being relatively small compared to the vdW interaction (20% *vs.* 80%, respectively). All these data confirm that the functionalization/de-fluorination of FMOF-1c to MeMOF-1c (*i.e.*, replacing $-CF_3$ with $-CH_3$ groups) leads to increased adsorption energy.

Fig. 9 depicts the adsorbate positions in FMOFs after Baker's minimization.[63,64] The nearest distances between $CO_2\cdots F\_CF_3$ and $CH_4\cdots F\_CF_3$ are 3.88 and 4.45 Å, respectively, in FMOF-1c. On the other hand, the nearest distances between $CO_2\cdots H\_CH_3$ and $CH_4\cdots H\_CH_3$ are 3.18 and 3.82 Å, respectively, in MeMOF-1c after minimization. Apparently, CO_2 and CH_4 molecules are much closer to H_CH_3 in MeMOF-1c than to F_CF_3 in FMOF-1c, with the values of 0.70 and 0.63 Å, respectively. It should be noted that the covalent radii of F and H are 0.71 and 0.37 Å, respectively.[81] Given that the differences between the guest···H and guest···F distances (0.70 and 0.63 Å) are higher than the difference between the covalent radii of F and H (0.34 Å), these results suggest genuinely stronger interactions of both adsorbates with MeMOF than with FMOF adsorbents.

3.4 Isotherm models

The adsorption isotherms obtained from molecular simulations were fitted using three different models: Langmuir, Langmuir–Freundlich (L–F), and Tóth models. The goodness-of-fit for each model with respect to the adsorption isotherms was assessed using the residual root-mean-square error (RMSE) and the chi-square test (χ^2). Further details can be found in the ESI.† Fig. S28–S30† depict the fitting curves of adsorbates for FMOF-1c at 288, 298, and 308 K. The fitting parameters and goodness-of-fit parameters are presented in Tables S6 (Langmuir), S7 (Freundlich–Langmuir), and S8 (Tóth) for FMOF-1c.†

As summarized in Table S8,† the comparison of the a_T parameter at all temperatures suggests a_T (CO_2) > a_T (CH_4), indicating that CO_2 reaches saturation and exhibits a higher maximum uptake than CH_4. The pressure required by the gas to attain a stable point follows the order CH_4 > CO_2, as indicated by b_T, which is inversely proportional to the pressure needed for saturation. As a result, CO_2 adsorption is higher than CH_4 adsorption in the low-pressure region.

The smallest RMSE and χ^2 values for the Tóth model indicate the best fitting for CO_2 and CH_4 isotherms in FMOF-1c compared to the other models. For CO_2, the Langmuir model underestimates the uptake between 1.0×10^6 Pa and 3.0×10^6 Pa while it overpredicts at very low and high-pressure regions. All models show better fitting for CH_4 than for CO_2. From the Tóth model for FMOF-1c, we observe a deviation of the heterogeneity parameter from unity, suggesting that FMOF-1c acts as a heterogenous surface during adsorption for both adsorbates. The same conclusion can be drawn while comparing the models for MeMOF-1c, as shown in Fig. S49–S51, and from the fitting parameters given in Tables S9 (Langmuir), S10 (Langmuir–Freundlich), and S11 (Tóth).†

The isosteric heats of adsorption at infinite dilution (Q_{st0}) were calculated using the Clausius–Clapeyron equation[82] (ESI†) based on the pure component CO_2 and CH_4 adsorption isotherms at 288, 298, and 308 K obtained by GCMC simulation. Since the Tóth model provided the best characterization of CO_2 and CH_4 adsorption in MOFs, we used the Tóth model parameters to generate pressure (p)/loading (n) pairs to estimate the Q_{st0} values. We compared the values of isosteric heats of adsorption at infinite dilution (Q_{st0}) obtained from

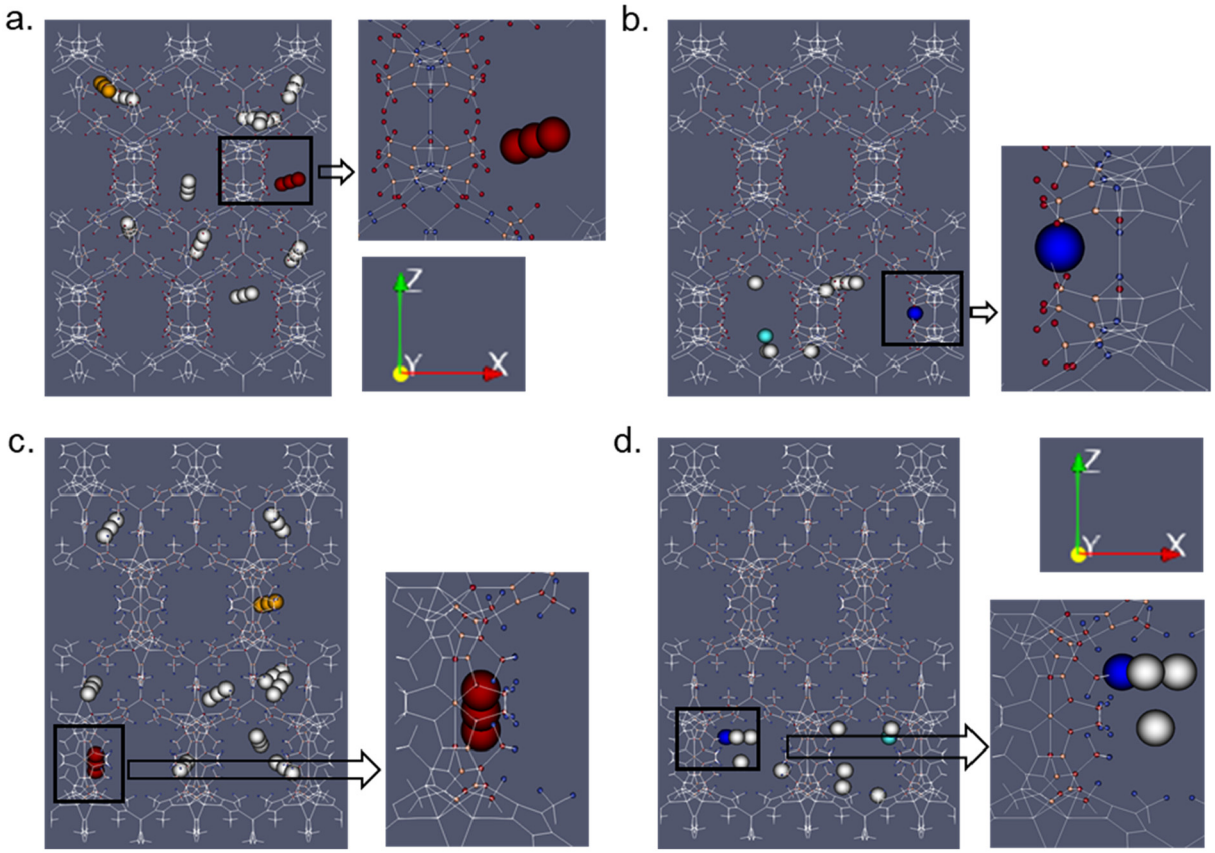

Fig. 9 Adsorption sites of (a) CO_2 and (b) CH_4 in FMOF-1c and (c) CO_2 and (d) CH_4 in MeMOF-1c. Initial and final (after minimization) positions of CO_2 are represented by orange and dark-red spheres, respectively, while analogous symbols for CH_4 are shown as cyan and dark-blue spheres, respectively; gray spheres represent different positions of molecules during minimization, with some points omitted for clarity purposes.

the Clausius–Clapeyron equation to those acquired from MC simulation (using the Widom insertion method) at different temperatures (Table 3). The results are comparable for CH_4, while for CO_2, the Q_{st0} values obtained from the Clausius–Clapeyron method are higher. It is worth mentioning that our calculated Q_{st0} value for CO_2 at 298 K in FMOF-1c (16.95 kJ mol^{-1}) using the Clausius–Clapeyron equation is comparable to the reported value (16.49 kJ mol^{-1})[69] found in the literature.

We also compared Henry's constants of CO_2 and CH_4 obtained from the Widom insertion method[62] using RASPA2 ($K_{H,\ RASPA}$) with the values ($K_{H,\ Tóth}$) calculated from the slope of the isotherms generated using the Tóth parameters in the low-pressure regime. Fig. S70–S73† depict the pressure range used for K_H calculations in MOFs, and the results are summarized in Table S12,† showing a satisfactory agreement between the two sets of values.

3.5 Interaction energies from DFT calculations

Density functional theory (DFT)-based calculations were used to obtain the interaction energy (IE) of the adsorbates (CO_2 and CH_4) with $-CF_3$ in FMOF-1c and $-CH_3$ in MeMOF-1c (Table 4 and Fig. 10a–d). The density functional B97D and the CEP-31G basis set were used in this study with the Gaussian16 code.[66] Only the triazole bearing two $-CF_3$ or two $-CH_3$ substituents at the 3,5-positions was used in the molecular model

Table 3 Q_{st0} (kJ mol^{-1}) for CO_2 and CH_4 adsorption in FMOF-1c and MeMOF-1c

Guest	Adsorbent	Q_{st0} (Clausius–Clapeyron)	Q_{st0} (MC/288 K)	Q_{st0} (MC/298 K)	Q_{st0} (MC/308 K)
CO_2	FMOF-1c	16.95	13.85 ± 2.56	13.71 ± 2.49	13.69 ± 2.41
	MeMOF-1c	30.58	25.15 ± 2.67	24.51 ± 2.61	23.95 ± 2.50
CH_4	FMOF-1c	11.28	11.60 ± 2.56	11.54 ± 2.48	11.48 ± 2.40
	MeMOF-1c	18.24	17.28 ± 2.64	17.02 ± 2.57	16.82 ± 2.47

Table 4 DFT-based (B97D/CEP-31G) interaction energy of CO_2 and CH_4 in small molecular models of FMOF and MeMOF

Adsorbate	Substituent	Interaction energy (kJ mol^{-1})
CO_2	$-CF_3$ (FMOF-1c)	−18.20
	$-CH_3$ (MeMOF-1c)	−22.46
CH_4	$-CF_3$ (FMOF-1c)	−6.00
	$-CH_3$ (MeMOF-1c)	−11.33

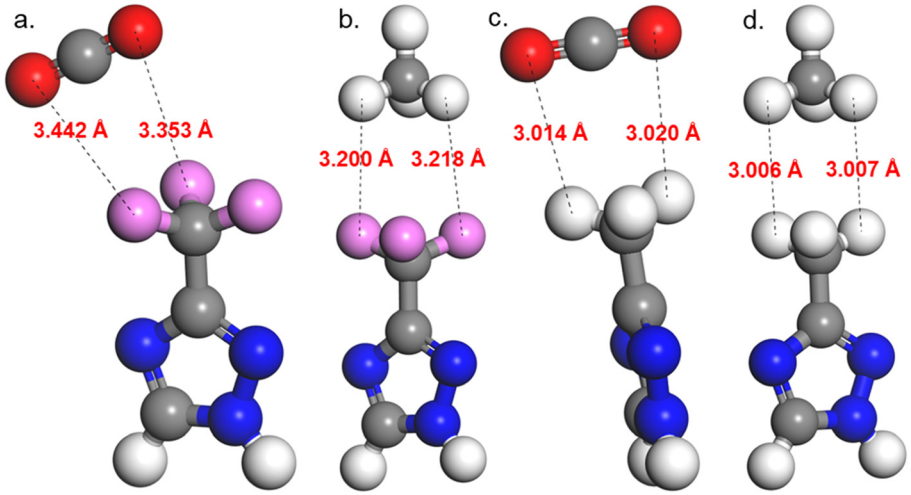

Fig. 10 DFT-optimized structures of the parent CF_3-substituted linker with (a) CO_2 and (b) CH_4 and the methyl-functionalized linker with (c) CO_2 and (d) CH_4. Color code – O: red, F: pink, N: blue, C: gray, and H: white.

for interaction with CO_2 or CH_4 (see Fig. 10), in order to make high-accuracy DFT computations that account for dispersion (physisorption/van der Waals interactions) feasible. For the convergence of the optimized structures, we examined the "Maximum Force" and "RMS Force" values within the optimization output, to make sure they fell below the predefined threshold values. In Gaussian 16, the default threshold values for "Maximum Force" and "RMS Force" during geometry optimization are typically set to 0.000450 Hartree $Bohr^{-1}$ and 0.000300 Hartree $Bohr^{-1}$, respectively. The lower values of "Maximum Force" and "RMS Force" than these threshold values ensured the convergence of the optimized structures, as shown in Fig. 10.

As per Table 4, the interaction energy of CO_2 is higher than that of CH_4 for both FMOF-1c and MeMOF-1c. It is also observed that $-CH_3$ functionalization affords stronger interactions with CO_2 and CH_4 compared to the parent $-CF_3$ functionalization. These results are consistent with the Q_{st0} values obtained either from MC simulations or *via* the Clausius–Clapeyron equation. The interaction energy between CO_2 and $-CH_3$ groups is -22.46 kJ mol^{-1}, which is comparable to the value reported by Gu *et al.*[83] The larger interaction energy of CO_2 compared to CH_4 can be ascribed, at least in part, to the quadrupole moment of CO_2.[84] We observe a smaller distance between O_CO_2 and H_CH_3 in comparison with O_CO_2 and F_CF_3, which also supports the aforementioned contention of stronger CO_2 interaction in MeMOFs than in FMOFs. The same analogy applies to CH_4 interaction, as suggested upon comparing the distances between H_CH_4 and F_CF_3 *vs.* H_CH_4 and H_CH_3, even after considering the covalent radius difference between F and H.

Given that the DFT calculations suggest a stronger interaction energy of CH_4 with the $-CH_3$ group in MeMOF-1 compared to the $-CF_3$ group in FMOF-1c, one may ascribe this to stronger interactions of CH_4 molecules with the $-CF_3$ groups due to the presence of a partial negative charge on the rather electronegative F atoms. In contrast, the H atoms in the $-CH_3$ group possess partial positive charges, and one might expect repulsive forces among the H atoms of the CH_4 molecule and those of the $-CH_3$ group. However, the calculations indicate an attractive C–H···H–C interaction (even stronger than the C–F···H–C interaction), which is not surprising. This could be explained by the dispersion stabilization of CH_4 molecules based on the valence bond (VB) model, as studied by Danovich *et al.*[85] The VB analysis revealed that the stabilization of C^+–H^-···H^+–C^- interaction arises due to the alternation of atomic charges (*i.e.*, $C^-H^+\cdots H^-C^+$ and C–H···H–C), thereby leading to an electrostatic interaction. This phenomenon is consistent with the classical mechanism of oscillating dipoles as the source of dispersion interactions. The presence of attractive C–H···H–C interactions was further confirmed by other researchers based on theoretical calculations using "quantum theory of atoms in molecules" (QTAIM) in planar aromatic systems.[86–90]

3.6 Selectivity and hydrophobicity of the MOFs

We investigated MeMOFs and FMOFs for their selective adsorption of CO_2 and CH_4 over water. As shown in Fig. S74,† the CO_2 and CH_4 adsorption selectivity values over water were comparable, obtained using two different methods (discussed in section 2.3; *vide supra*) for FMOF-1c at 298 K. The selectivity of CO_2 over water in FMOF-1c is 6.4, derived from GCMC simulations, whereas the value acquired from Henry's constant ratio is 6.5. The selectivity of CH_4 over water in FMOF-1c is 4.3 and 3.9 obtained from GCMC simulations and Henry's constant ratio, respectively. The CO_2/H_2O selectivity using GCMC simulations was examined for a binary mixture of CO_2 and H_2O ($CO_2 : H_2O = 7 : 2$ at 80% RH, corresponding to 3280 Pa) at 0.15 bar and 298 K. For CH_4/H_2O selectivity, we modeled a binary mixture of CH_4 and H_2O at 95% RH, 1 bar and 298 K.

The CO_2/H_2O and CH_4/H_2O selectivity for a set of MOFs was calculated using their Henry's constant ratios, as shown in Fig. 11. We compared the results of different FMOF and

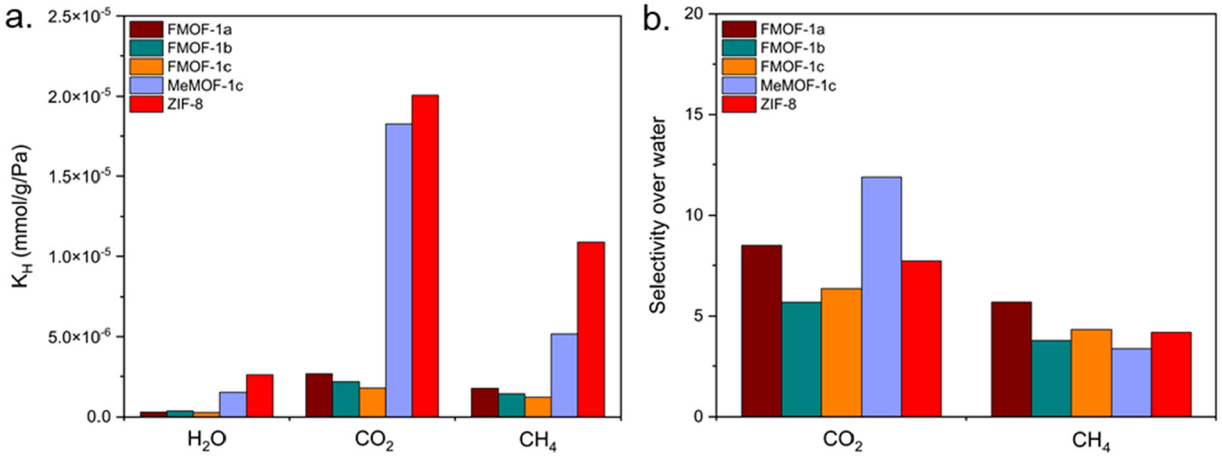

Fig. 11 (a) Henry's constant (K_H) for H_2O, CO_2, and CH_4 at 298 K; (b) adsorption selectivity of CO_2 and CH_4 over water for various MOFs at 298 K.

MeMOF structures with those of a prototypical hydrophobic MOF, ZIF-8. The K_H values of CO_2, CH_4, and H_2O in ZIF-8 from our simulations are 2.01 × 10^{-5} mmol g^{-1} Pa^{-1}, 1.09 × 10^{-5} mmol g^{-1} Pa^{-1} and 2.61 × 10^{-6} mmol g^{-1} Pa^{-1}, respectively. These values are comparable to those obtained by Moghadam *et al.*[91] – namely 1.50 × 10^{-5} mmol g^{-1} Pa^{-1} for CH_4 and 2.60 × 10^{-6} mmol g^{-1} Pa^{-1} for H_2O – suggesting good validation for our methodology. Overall, the results suggest that ZIF-8 has the largest K_H values for "dry" CO_2 and CH_4, as expected for such a high-surface-area standard hydrophobic framework.

The highest selectivity for CO_2 over H_2O was obtained for MeMOF-1c with a value of 11.9. ZIF-8 shows the largest K_H for H_2O among all the hydrophobic structures investigated. The higher CO_2/H_2O selectivity of MeMOF-1c compared to ZIF-8 is due to the relatively lower K_H value for H_2O adsorption in MeMOF-1c compared to that in ZIF-8. On the other hand, FMOF-1a shows the highest selectivity for CH_4 over H_2O – likely due to its lowest K_H value for H_2O adsorption. The CH_4/H_2O selectivity was 5.7 for FMOF-1a, which is higher compared to ZIF-8, whereas all other structures showed comparatively lower values.

The simulated pure component water adsorption isotherms are presented in Fig. 12 for both the parent $-CF_3$ and the $-CH_3$ functionalized MOFs at 298 K. As water interaction is highly sensitive to the charges of framework atoms, we used two different charge methods, CBAC[56] and EQeq,[71] to predict the water adsorption isotherms of the adsorbents. A Type V water adsorption profile was observed for MeMOF-1c, indicating the presence of weak interactions between the adsorbate and the adsorbent, using the CBAC method. The water condensation pressure, P_c, for MeMOF-1c was found to be 4500 Pa, close to saturation. In contrast, these simulations do not predict any water condensation in MeMOF-1c based on the EQeq method. Likewise, no water condensation pressure was found for FMOF-1c. Fig. S75† shows the number of water molecules adsorbed in FMOF-1c at 298 K and 4500 Pa as a function of the number of MC cycles. This graph confirms the water convergence in hydrophobic FMOF structures, and thus, we conclude that the water adsorption isotherms shown in Fig. 12 are reliable.

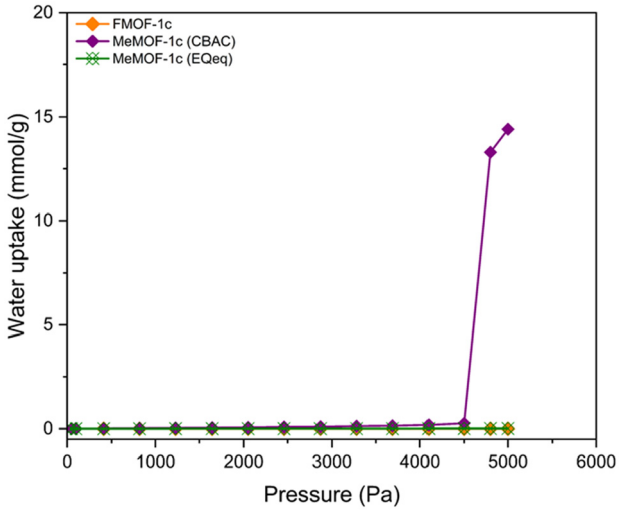

Fig. 12 Water uptake for FMOF-1c and MeMOF-1c at 298 K.

Lastly, we used GCMC simulations to model a binary mixture of CH_4 and water at 80% relative humidity to examine the influence of water/high humidity on CH_4 uptake in FMOF-1c (Fig. 13) and MeMOF-1c (Fig. 14). The isotherms show similar CH_4 uptake under both dry and wet conditions, demonstrating negligible loss of CH_4 uptake at 80% relative humidity in FMOF-1c. The impact of humidity on CO_2 and CH_4 adsorption in MeMOF-1c was also considered to study the effect of $-CH_3$ functionalization on CO_2 and CH_4 uptake under humid conditions (Fig. 14). Thus, GCMC simulations were performed to obtain excess adsorption isotherms for pure-component CO_2 and CH_4 as well as binary mixtures of CO_2/H_2O and CH_4/H_2O at 80% RH and 298 K in MeMOF-1c (Fig. 14). MeMOF-1c exhibits a much higher uptake of CO_2 and CH_4 than H_2O. Although the interaction of H_2O with the methyl-functionalized MOF, MeMOF-1c, is higher than that with the

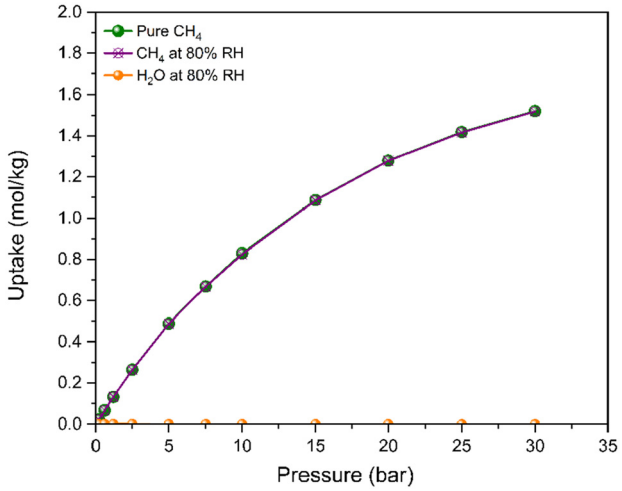

Fig. 13 Adsorption isotherms of pure component CH_4 and a binary mixture of CH_4 and H_2O at 80% relative humidity in FMOF-1c at 298 K.

parent MOF, FMOF-1c, this higher H_2O interaction did not significantly affect the CO_2 and CH_4 uptake in MeMOF-1c at 80% RH (Fig. 14). We speculate that this nominal influence on CO_2 and CH_4 uptake in MeMOF-1c is due to the lower partial pressure of water (3280 Pa) than the observed water condensation pressure (4500 Pa). We simulated the 80% RH by fixing the partial pressure of water at 3280 Pa throughout the isotherm, based on the vapor pressure (4100 Pa) predicted by the TIP4P water model. As shown in Fig. 12, water condensation occurs at 4500 Pa, which is higher than the partial pressure of water (3280 Pa) in the binary mixture.

3.7 Experimental validation of the PXRD pattern and superhydrophobicity of MeMOFs

The successful synthesis of a MeMOF-2 composition, corresponding to the {Ag(3,5-$(CH_3)_2$-1,2,4-triazolate)} empirical formula of the simulated structures, was confirmed by powder X-ray diffraction (PXRD). The PXRD pattern for this synthesized material, however, corresponded to a different crystal structure pattern published by Zhai *et al.*[67] The two patterns show excellent agreement, as shown in Fig. 15a.

It should be noted that the structure of the simulated MeMOF-1 and the synthesized MeMOF-2 are dissimilar, as revealed by the PXRD pattern in Fig. 15b, but more similar to the analogous FMOF-1 structure even after the $-CF_3 \rightarrow -CH_3$ replacement. This underscores the complexity of predicting the structure of the actual polymorph upon synthesis guided by such simulations. Despite this, the retention of the predicted hydrophobic properties in the synthesized compound, based on contact angle measurements (Fig. 16), suggests that the underlying design principles are still valuable. A crystal structure or PXRD pattern with the same $Ag_2[Ag_4Tz_6]$ unit cell formula and topology as the simulated hypothetical structures for MeMOF-1a/1b/1c, which correspond to the analogous FMOF-1a/1b/1c experimental structures, has not yet been isolated. Also, GCMC simulations of $CH_4/CO_2/H_2O$ adsorption for the experimental structure of MeMOF-2 that we have synthesized, which corresponds to that reported by Zhai *et al.*,[67] are not feasible because of the very low porosity of this experimental structure compared to MeMOF-1a/1b/1c hypothetical structures. Nevertheless, the simulations for the hypothetical structures are still valuable, not only in anticipation of the culmination of our ongoing efforts to isolate these or other porous structures experimentally, but also for the experimental and other possible low-porosity MeMOF-2 compositions corresponding to the same {Ag(3,5-$(CH_3)_2$-1,2,4-triazolate)} empirical formula. This is because the guest adsorption and water repulsion attributes are generally a function of the surface interaction energy between a given guest molecule and the surface functional group of the MOF, which is minimally dependent on porosity. This is validated by the general agreement between the DFT simulations for CH_4/CO_2 with the 3,5-

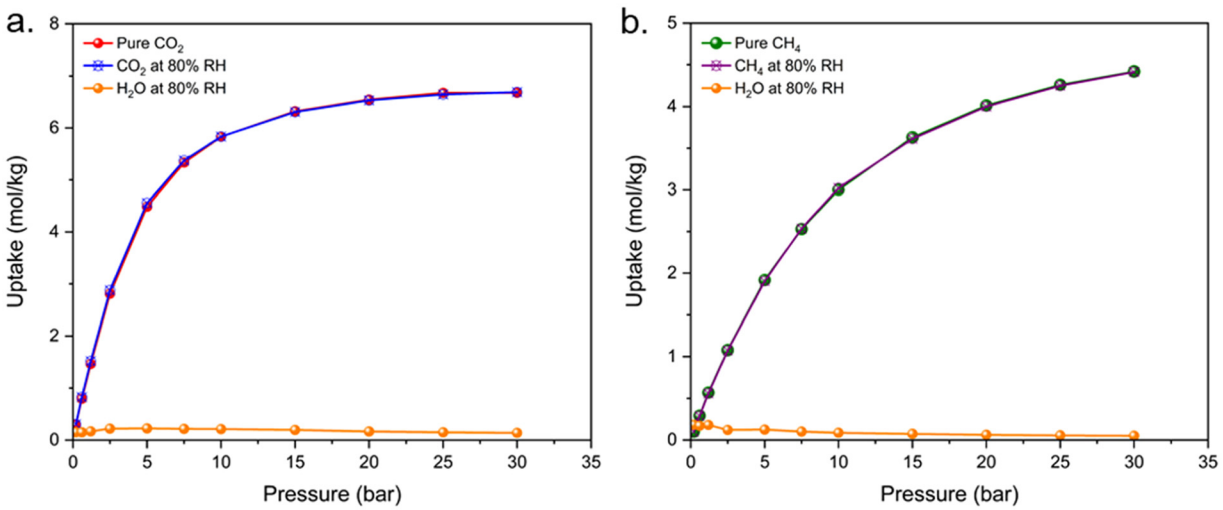

Fig. 14 Adsorption isotherms of (a) pure component CO_2 and a binary mixture of CO_2 and H_2O at 80% relative humidity and (b) pure component CH_4 and a binary mixture of CH_4 and H_2O at 80% relative humidity in MeMOF-1c at 298 K.

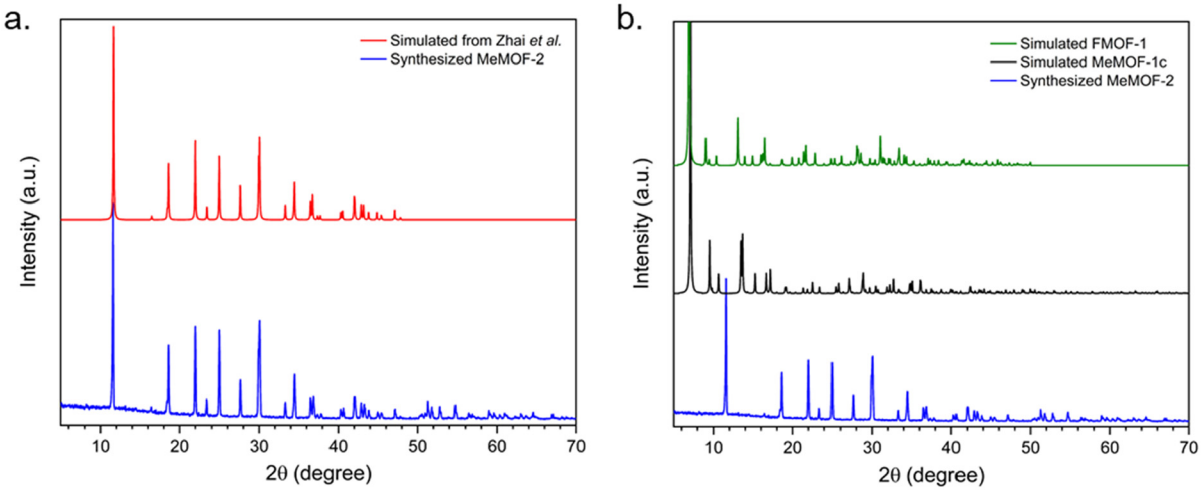

Fig. 15 (a) PXRD pattern of the synthesized MeMOF-2 in this work (blue) overlaid with the published PXRD pattern by Zhai *et al.* (red)[67] and (b) experimental PXRD pattern of the MeMOF-2 sample experimentally prepared herein (blue) overlaid with the simulated PXRD patterns corresponding to the experimental crystal structure of FMOF-1 [45] (green) and its hypothetical MeMOF-1c analogue (black).

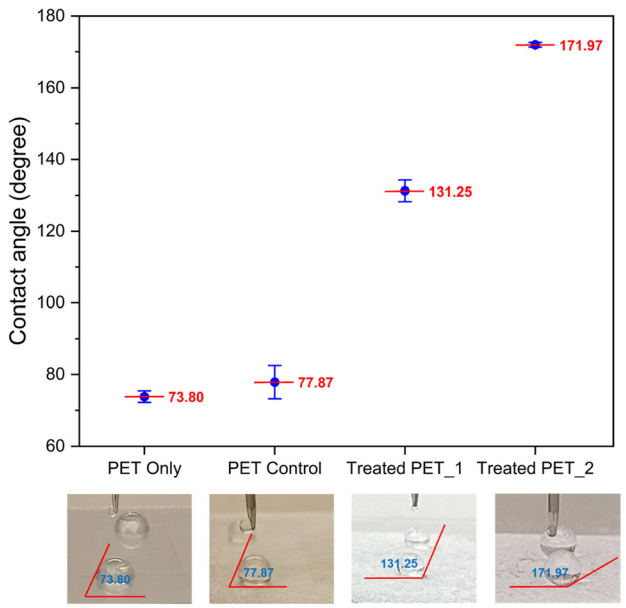

Fig. 16 Water-drop contact angle data for PET only, PET control (sanded), treated PET_1 (FMOF-1@PET), and treated PET_2 (MeMOF-2@PET) from left-to-right, respectively. Contact angle values are shown as average ± standard deviation from triplicate (n = 3) measurements.

$(CH_3)_2$-1,2,4-TzH ligand in Table 4 and the GCMC-derived Q_{st0} values in Tables 2 and 3 (with analogous comparisons for FMOF-1 [37], further validated by experimental Q_{st} values). Furthermore, Galli *et al.*[39] reported that another water repulsion metric, low-κ (dielectric constant) at high humidity, was sustained and even slightly enhanced for FMOF-1 samples when pressed at very high pressure, rendering them amorphous instead of crystalline (hence greatly reducing their porosity).

We have sought experimental validation of the GCMC-predicted hydrophobicity of the MeMOF-2 composition, $[Ag(Me_2Tz)]_\infty$. As shown in Fig. 16, the PET plastic substrate exhibits an increase in water-drop contact angle by ~100°, from ~74° (merely hydrophobic) to ~172° (superhydrophobic). This contact angle for MeMOF-2@PET is similar to, and indeed slightly higher than, that (~160°) we reported for a neat pellet of FMOF-1 formed spontaneously after the high-pressure CO_2 adsorption experiment[37] and significantly higher than that for the FMOF-1@PET sample (~131°) tested herein under the same conditions for comparison.

4. Conclusions

GCMC simulations were performed to study the CO_2 and CH_4 adsorption isotherms at three different temperatures (288, 298, and 308 K) in the parent, FMOF-1, and analogous methyl-functionalized MeMOF-1 structures, where $-CF_3$ groups in FMOF-1 were replaced by $-CH_3$, using a force field that has been validated. The thermodynamic parameters (Henry's constants and isosteric heat of adsorption at infinite dilution) were obtained directly from MC simulations (using the Widom insertion method). The adsorption isotherms generated by molecular simulations were fitted to the Langmuir, Freundlich–Langmuir, and Tóth models. The Tóth model showed the best fit for both CO_2 and CH_4 in FMOF-1 and MeMOF-1 at all three aforementioned temperatures, as indicated by the lower residual root-mean-square error and chi-square values. Our results for Henry's constants (K_H) and isosteric heat of adsorption at infinite dilution (Q_{st0}), obtained either during the simulation or by using the Tóth isotherm model, are highly consistent and demonstrate that CO_2 and CH_4 have a greater affinity for MeMOF-1 than for FMOF-1, and for the same MOF, the order is CO_2 > CH_4, as indicated by the

higher K_H and Q_{st0} values. The larger uptake of CO_2 and CH_4 in MeMOF-1 predicted by GCMC simulations is attributed to the effect of $-CH_3$ functionalization of FMOF-1. The selectivity and hydrophobicity were also investigated. The findings showed that water either does not condense at all, in one model, or condenses near saturation at 4500 Pa in another model, in MeMOF-1, similar to the FMOF-1c behavior, which exhibited no water condensation in either model. Most importantly, no loss of CO_2 or CH_4 uptake was observed at 80% RH in the methyl-functionalized MOFs. Hence, MeMOF-1 is a promising candidate for CO_2 and CH_4 capture under humid conditions, suggesting that MeMOFs are potential fluorine-free superhydrophobic alternatives to FMOF, ZIF, Teflon, and PFAS materials. Finally, proof-of-concept experimental data validated the superhydrophobic nature of the MeMOF-2 composition, which increased the water-drop contact angle from ~74° to ~172° upon dry-coating a plastic substrate with MeMOF-2.

Data availability

The data supporting this article have been included as part of the ESI.†

Conflicts of interest

The authors declare no conflict of interest.

Acknowledgements

M. A. O. acknowledges support from the U.S. Nuclear Regulatory Commission (award 31310023M0019), the U.S. Department of Defense (award W911NF2210201), the Welch Foundation (B-1542), and the U.S. National Science Foundation (CHE-1413641 and an international supplement thereof, CHE-1545934). J. D. acknowledges support for his group's contribution from the U.S. National Science Foundation (CMMI-1662288) and in part from the Advanced Research Projects Agency-Energy (ARPA-E) of the U.S. Department of Energy (DE AR0001613). The computational facilities have been supported by the National Science Foundation (CHE-1531468 and OAC-2117247) and the University of North Texas (Research Computing Services and Texas Advanced Computing Center).

References

1 J. Liu, P. K. Thallapally, B. P. McGrail, D. R. Brown and J. Liu, *Chem. Soc. Rev.*, 2012, **41**, 2308–2322.
2 D. L. Royer, R. A. Berner and J. Park, *Nature*, 2007, **446**, 530–532.
3 B. Metz, O. Davidson, H. C. De Coninck, M. Loos and L. Meyer, *IPCC Special Report on Carbon Dioxide Capture and Storage*, Cambridge University Press, Cambridge, United Kingdom, 2005.
4 D. R. Feldman, W. D. Collins, P. J. Gero, M. S. Torn, E. J. Mlawer and T. R. Shippert, *Nature*, 2015, **519**, 339–343.
5 *Inventory of U.S. Greenhouse gas Emissions and Sinks: 1990–1994*, U. S. Environmental Protection Agency. Office of Policy, Planning and Evaluation, Washington, D.C., U.S. A, 1995.
6 L. Li, J. Yang, J. Li, Y. Chen and J. Li, *CrystEngComm*, 2013, **15**, 6782.
7 J. Park, H. Cha, S. Song and K. M. Chun, *Int. J. Hydrogen Energy*, 2011, **36**, 5153–5162.
8 K. Sumida, D. L. Rogow, J. A. Mason, T. M. McDonald, E. D. Bloch, Z. R. Herm, T.-H. Bae and J. R. Long, *Chem. Rev.*, 2012, **112**, 724–781.
9 J. Yu, S. Wang and H. Yu, *Int. J. Greenhouse Gas Control*, 2016, **50**, 135–146.
10 G. T. Rochelle, *Science*, 2009, **325**, 1652–1654.
11 Y. Lin, *Curr. Opin. Chem. Eng.*, 2015, **8**, 21–28.
12 J. Y. S. Lin, *Science*, 2016, **353**, 121–122.
13 Y. Wu, X. Chen, M. Fan, G. Jiang, Y. Kong and A. E. Bland, *Chem. Eng. J.*, 2015, **262**, 1192–1198.
14 Q. Yang, C. Zhong and J.-F. Chen, *J. Phys. Chem. C*, 2008, **112**, 1562–1569.
15 S. Yang, Z. Liu, X. Yan, C. Liu, Z. Zhang, H. Liu and L. Chai, *Energy Fuels*, 2019, **33**, 11380–11388.
16 J. Hu, Y. Liu, J. Liu and C. Gu, *AIChE J.*, 2020, **66**(2), e16835.
17 D. M. D'Alessandro, B. Smit and J. R. Long, *Angew. Chem., Int. Ed.*, 2010, **49**, 6058–6082.
18 G. Férey, *Chem. Soc. Rev.*, 2008, **37**, 191–214.
19 J. R. Long and O. M. Yaghi, *Chem. Soc. Rev.*, 2009, **38**, 1213.
20 A. Pal, S. Chand and M. C. Das, *Inorg. Chem.*, 2017, **56**, 13991–13997.
21 J. L. C. Rowsell and O. M. Yaghi, *J. Am. Chem. Soc.*, 2006, **128**, 1304–1315.
22 Y. F. Chen, A. Nalaparaju, M. Eddaoudi and J. W. Jiang, *Langmuir*, 2012, **28**, 3903–3910.
23 S. Li, Y. G. Chung, C. M. Simon and R. Q. Snurr, *J. Phys. Chem. Lett.*, 2017, **8**, 6135–6141.
24 J. An and N. L. Rosi, *J. Am. Chem. Soc.*, 2010, **132**, 5578–5579.
25 X.-J. Wang, P.-Z. Li, Y. Chen, Q. Zhang, H. Zhang, X. X. Chan, R. Ganguly, Y. Li, J. Jiang and Y. Zhao, *Sci. Rep.*, 2013, **3**, 1149.
26 X. Liu, M. Park, S. Hong, M. Oh, J. W. Yoon, J.-S. Chang and M. S. Lah, *Inorg. Chem.*, 2009, **48**, 11507–11509.
27 K. K. Tanabe and S. M. Cohen, *Chem. Soc. Rev.*, 2011, **40**, 498–519.
28 J. Hu, Y. Liu, J. Liu and C. Gu, *Fuel*, 2017, **200**, 244–251.
29 Z. Xiang, S. Leng and D. Cao, *J. Phys. Chem. C*, 2012, **116**, 10573–10579.
30 B. Zheng, J. Bai, J. Duan, L. Wojtas and M. J. Zaworotko, *J. Am. Chem. Soc.*, 2011, **133**, 748–751.
31 J. An, S. J. Geib and N. L. Rosi, *J. Am. Chem. Soc.*, 2010, **132**, 38–39.

32 Y. Ye, H. Zhang, L. Chen, S. Chen, Q. Lin, F. Wei, Z. Zhang and S. Xiang, *Inorg. Chem.*, 2019, **58**, 7754–7759.
33 J. Liu, A. I. Benin, A. M. B. Furtado, P. Jakubczak, R. R. Willis and M. D. LeVan, *Langmuir*, 2011, **27**, 11451–11456.
34 A. C. Kizzie, A. G. Wong-Foy and A. J. Matzger, *Langmuir*, 2011, **27**, 6368–6373.
35 S. Keskin, T. M. van Heest and D. S. Sholl, *ChemSusChem*, 2010, **3**, 879–891.
36 H. Furukawa, F. Gándara, Y.-B. Zhang, J. Jiang, W. L. Queen, M. R. Hudson and O. M. Yaghi, *J. Am. Chem. Soc.*, 2014, **136**, 4369–4381.
37 P. Z. Moghadam, J. F. Ivy, R. K. Arvapally, A. M. dos Santos, J. C. Pearson, L. Zhang, E. Tylianakis, P. Ghosh, I. W. H. Oswald, U. Kaipa, X. Wang, A. K. Wilson, R. Q. Snurr and M. A. Omary, *Chem. Sci.*, 2017, **8**, 3989–4000.
38 C. Yang, U. Kaipa, Q. Z. Mather, X. Wang, V. Nesterov, A. F. Venero and M. A. Omary, *J. Am. Chem. Soc.*, 2011, **133**, 18094–18097.
39 S. Galli, A. Cimino, J. F. Ivy, C. Giacobbe, R. K. Arvapally, R. Vismara, S. Checchia, M. A. Rawshdeh, C. T. Cardenas, W. K. Yaseen, A. Maspero and M. A. Omary, *Adv. Funct. Mater.*, 2019, **29**(40), 1904707.
40 T.-H. Chen, I. Popov, O. Zenasni, O. Daugulis and O. Š. Miljanić, *Chem. Commun.*, 2013, **49**, 6846.
41 Z. Zhang and O. Š. Miljanić, *Org. Mater.*, 2019, **01**, 019–029.
42 Z. Zhang, T. Lieu, C.-H. Wu, X. Wang, J. I. Wu, O. Daugulis and O. Š. Miljanić, *Chem. Commun.*, 2019, **55**, 9387–9390.
43 Z. Yang, S. Wang, Z. Zhang, W. Guo, K. Jie, M. I. Hashim, O. Š. Miljanić, D. Jiang, I. Popovs and S. Dai, *J. Mater. Chem. A*, 2019, **7**, 17277–17282.
44 T.-H. Chen, I. Popov, W. Kaveevivitchai, Y.-C. Chuang, Y.-S. Chen, O. Daugulis, A. J. Jacobson and O. Š. Miljanić, *Nat. Commun.*, 2014, **5**, 5131.
45 C. Yang, X. Wang and M. A. Omary, *J. Am. Chem. Soc.*, 2007, **129**, 15454–15455.
46 Accelrys Software Inc., Material Studio Modeling Environment, Release 6, Accelrys Software Inc., San Diego, California, USA, 2011.
47 A. K. Rappe, C. J. Casewit, K. S. Colwell, W. A. Goddard and W. M. Skiff, *J. Am. Chem. Soc.*, 1992, **114**, 10024–10035.
48 D. A. Gomez-Gualdron, O. V. Gutov, V. Krungleviciute, B. Borah, J. E. Mondloch, J. T. Hupp, T. Yildirim, O. K. Farha and R. Q. Snurr, *Chem. Mater.*, 2014, **26**, 5632–5639.
49 O. K. Farha, A. Özgür Yazaydın, I. Eryazici, C. D. Malliakas, B. G. Hauser, M. G. Kanatzidis, S. T. Nguyen, R. Q. Snurr and J. T. Hupp, *Nat. Chem.*, 2010, **2**, 944–948.
50 O. V. Gutov, W. Bury, D. A. Gomez-Gualdron, V. Krungleviciute, D. Fairen-Jimenez, J. E. Mondloch, A. A. Sarjeant, S. S. Al-Juaid, R. Q. Snurr, J. T. Hupp, T. Yildirim and O. K. Farha, *Chem. – Eur. J.*, 2014, **20**, 12389–12393.
51 T. Düren, Y.-S. Bae and R. Q. Snurr, *Chem. Soc. Rev.*, 2009, **38**, 1237.
52 J. G. McDaniel, S. Li, E. Tylianakis, R. Q. Snurr and J. R. Schmidt, *J. Phys. Chem. C*, 2015, **119**, 3143–3152.
53 D. Frenkel and B. Smit, *Understanding Molecular Simulation: From Algorithm to Applications*, Elsevier Inc., 3rd edn, 2023.
54 P. P. Ewald, *Ann. Phys.*, 1921, **369**, 253–287, DOI: **10.1002/andp.19213690304**.
55 V. H. Dalvi, V. Srinivasan and P. J. Rossky, *J. Phys. Chem. C*, 2010, **114**, 15553–15561.
56 Q. Xu and C. Zhong, *J. Phys. Chem. C*, 2010, **114**, 5035–5042.
57 J. J. Potoff and J. I. Siepmann, *AIChE J.*, 2001, **47**, 1676–1682.
58 A. M. Fracaroli, H. Furukawa, M. Suzuki, M. Dodd, S. Okajima, F. Gándara, J. A. Reimer and O. M. Yaghi, *J. Am. Chem. Soc.*, 2014, **136**, 8863–8866.
59 W. L. Jorgensen, J. Chandrasekhar, J. D. Madura, R. W. Impey and M. L. Klein, *J. Chem. Phys.*, 1983, **79**, 926–935.
60 D. Dubbeldam, S. Calero, D. E. Ellis and R. Q. Snurr, *Mol. Simul.*, 2016, **42**, 81–101.
61 D.-Y. Peng and D. B. Robinson, *Ind. Eng. Chem. Fundam.*, 1976, **15**, 59–64.
62 B. Widom, *J. Chem. Phys.*, 1963, **39**, 2808–2812.
63 S. Grimme, S. Ehrlich and L. Goerigk, *J. Comput. Chem.*, 2011, **32**, 1456–1465.
64 J. Baker, *J. Comput. Chem.*, 1986, **7**, 385–395.
65 T. F. Willems, C. H. Rycroft, M. Kazi, J. C. Meza and M. Haranczyk, *Microporous Mesoporous Mater.*, 2012, **149**, 134–141.
66 M. J. Frisch, G. W. Trucks, H. B. Schlegel, G. E. Scuseria, M. A. Robb, J. R. Cheeseman, G. Scalmani, V. Barone, G. A. Petersson, H. Nakatsuji, X. Li, M. Caricato, A. V. Marenich, J. Bloino, B. G. Janesko, R. Gomperts, B. Mennucci, H. P. Hratchian, J. V. Ortiz, A. F. Izmaylov, J. L. Sonnenberg, D. Williams-Young, F. Ding, F. Lipparini, F. Egidi, J. Goings, B. Peng, A. Petrone, T. Henderson, D. Ranasinghe, V. G. Zakrzewski, J. Gao, N. Rega, G. Zheng, W. Liang, M. Hada, M. Ehara, K. Toyota, R. Fukuda, J. Hasegawa, M. Ishida, T. Nakajima, Y. Honda, O. Kitao, H. Nakai, T. Vreven, K. Throssell, J. A. Montgomery Jr., J. E. Peralta, F. Ogliaro, M. J. Bearpark, J. J. Heyd, E. N. Brothers, K. N. Kudin, V. N. Staroverov, T. A. Keith, R. Kobayashi, J. Normand, K. Raghavachari, A. P. Rendell, J. C. Burant, S. S. Iyengar, J. Tomasi, M. Cossi, J. M. Millam, M. Klene, C. Adamo, R. Cammi, J. W. Ochterski, R. L. Martin, K. Morokuma, O. Farkas, J. B. Foresman and D. J. Fox, *Gaussian 16, Revision C.01*, Gaussian, Inc., Wallingford CT, 2016.
67 Q.-G. Zhai, M.-C. Hu, S.-N. Li and Y.-C. Jiang, *Inorg. Chim. Acta*, 2009, **362**, 1355–1357.
68 W. Chen, W. Wang, D. X. Luong, J. T. Li, V. Granja, P. A. Advincula, C. Ge, Y. Chyan, K. Yang, W. A. Algozeeb, C. F. Higgs and J. M. Tour, *ACS Appl. Mater. Interfaces*, 2022, **14**, 35053–35063.
69 R. Babarao and J. Jiang, *Langmuir*, 2008, **24**, 6270–6278.

70 N. Nijem, P. Canepa, U. Kaipa, K. Tan, K. Roodenko, S. Tekarli, J. Halbert, I. W. H. Oswald, R. K. Arvapally, C. Yang, T. Thonhauser, M. A. Omary and Y. J. Chabal, *J. Am. Chem. Soc.*, 2013, **135**, 12615–12626.
71 C. E. Wilmer, K. C. Kim and R. Q. Snurr, *J. Phys. Chem. Lett.*, 2012, **3**, 2506–2511.
72 S. M. S. Islam, R. Yasmeen, G. Verma, S. M. Tekarli, V. N. Nesterov, S. Ma and M. A. Omary, *Inorg. Chem.*, 2024, **63**, 8664–8673.
73 H. W. B. Teo, A. Chakraborty and S. Kayal, *Appl. Therm. Eng.*, 2017, **110**, 891–900.
74 R. Yasmeen, S. M. S. Islam, J. Du and M. Omary, *Dalton Trans.*, 2025, DOI: **10.1039/D4DT03093A**.
75 K. A. Forrest, T. Pham, A. Hogan, K. McLaughlin, B. Tudor, P. Nugent, S. D. Burd, A. Mullen, C. R. Cioce, L. Wojtas, M. J. Zaworotko and B. Space, *J. Phys. Chem. C*, 2013, **117**, 17687–17698.
76 J. A. Mason, M. Veenstra and J. R. Long, *Chem. Sci.*, 2014, **5**, 32–51.
77 G. Xiong, B.-B. Wang, L.-X. You, B.-Y. Ren, Y.-K. He, F. Ding, I. Dragutan, V. Dragutan and Y.-G. Sun, *J. Mater. Chem. A*, 2019, **7**, 393–404.
78 C. E. Wilmer, O. K. Farha, Y.-S. Bae, J. T. Hupp and R. Q. Snurr, *Energy Environ. Sci.*, 2012, **5**, 9849.
79 T. Pham, K. A. Forrest, E. H. L. Falcão, J. Eckert and B. Space, *Phys. Chem. Chem. Phys.*, 2016, **18**, 1786–1796.
80 L. Qu, Z. Wang and L. Liu, *Fire*, 2023, **6**, 355.
81 *The periodic table of the elements*. WebElements. **https://webelements.com/** (accessed Feb 17, 2025).
82 H. Pan, J. A. Ritter and P. B. Balbuena, *Langmuir*, 1998, **14**, 6323–6327.
83 C. Gu, Y. Liu, W. Wang, J. Liu and J. Hu, *Front. Chem. Sci. Eng.*, 2021, **15**, 437–449.
84 R. Paulini, K. Müller and F. Diederich, *Angew. Chem., Int. Ed.*, 2005, **44**, 1788–1805.
85 D. Danovich, S. Shaik, F. Neese, J. Echeverría, G. Aullón and S. Alvarez, *J. Chem. Theory Comput.*, 2013, **9**, 1977–1991.
86 R. F. W. Bader, *Atoms in Molecules: A Quantum Theory*, Oxford University Press, Walton Street, Oxford, United Kingdom, 1990.
87 C. F. Matta, J. Hernández-Trujillo, T. Tang and R. F. W. Bader, *Chem. – Eur. J.*, 2003, **9**, 1940–1951.
88 J. Hernández-Trujillo and C. F. Matta, *Struct. Chem.*, 2007, **18**, 849–857.
89 L. F. Pacios and L. Gómez, *Chem. Phys. Lett.*, 2006, **432**, 414–420.
90 J. Echeverría, G. Aullón, D. Danovich, S. Shaik and S. Alvarez, *Nat. Chem.*, 2011, **3**, 323–330.
91 P. Z. Moghadam, D. Fairen-Jimenez and R. Q. Snurr, *J. Mater. Chem. A*, 2016, **4**, 529–536.